Applied Ocean Research 165 (2025) 104809

Contents lists available at ScienceDirect

Applied Ocean Research

journal homepage: www.elsevier.com/locate/apor

Research paper

Gaussian copula-based Bayesian Networks for dynamic loads in mooring systems

R. Santjer [a,b,*], S. Agarwal [c], O. Colomés [c], O. Morales-Nápoles [c]

[a] Department of Data Science and Waterquality, Deltares, Boussinesqweg 1, Delft, 2629 HV, The Netherlands
[b] Faculty of Electrical Engineering, Mathematics and Computer Science, Delft University of Technology, Mekelweg 4, Delft, 2628 CD, The Netherlands
[c] Faculty of Civil Engineering and Geosciences, Delft University of Technology, Stevinweg 1, Delft, 2628 CN, The Netherlands

ARTICLE INFO

Keywords:
Gaussian copula-based Bayesian Network
Copula models
Mooring system
Offshore floating structure
Snap loads

ABSTRACT

Offshore floating structures are experiencing harsh environmental conditions risking their safety. Therefore, mooring lines are crucial for ensuring structures' stability. Sudden increases in tensions after temporarily slack of the mooring line are called snap loads and are the most critical load states. These snap loads and their dependence to various factors are investigated in the present study. 12 study locations in the south-eastern North Sea are selected. For each location, wave and current variables are extracted from a three-dimensional large-scale numerical model covering the European Shelf. Mooring tensions at different rope positions are calculated via a Finite Element model for flexible mooring lines for different hydrodynamic conditions and used subsequently to obtain tension rates as indicator for snap loads. The dependence among 13 variables per study location is modelled via Gaussian copula-based Bayesian Networks (GCBN). This allows for spatial analysis of the relationships between hydrodynamic variables and tension rates, but also to determine the influence of hydrodynamic variables on expected tension rates. Furthermore, distributions of tension rates are obtained under specific constant hydrodynamic conditions. The results indicate that conditionalising on certain hydrodynamic variables can reduce the expected tension rates, as their marginal distributions are characterised by heavy tails. Still, mooring systems should be designed conservatively. However, once specific hydrodynamic information is available, uncertainties can be minimised, enhancing safety and reliability. Thus, accounting for the dependence among hydrodynamic variables and tension rates is crucial for improving the safety of structures under varying environmental conditions.

1. Introduction

The offshore marine environment has enormous economic potential. For example as a source of renewable energy and proteins obtained from aquaculture. Thus, making efficient use of this space is increasingly important. Not only is there an increasing demand for proteins (Yong et al., 2022), but offshore wind energy is also expected to continue to grow in the coming years (Soares-Ramos et al., 2020). This in turn will help replacing energy production sectors based on fossil fuels and reducing carbon emissions, thus potentially contributing to limit global warming. Osman et al. (2023) reviewed several aspects of renewable energy under climate change. Prices for energy from offshore wind, biomass production, and other green energy sources are expected to drop drastically in the future while having a comparably minimal impact on the environment. However, the space at sea, especially near-shore, is limited and therefore there are conflicts between sectors and users (e.g., Buck and Langan, 2017; Pınarbaşı et al., 2017; Buck et al., 2018). These conflicts include spatial, environmental, and societal challenges, between traditional users such as fisheries, tourism, and ports. Unlike nearshore, offshore areas have different stakeholders and a lot of potential for multi-use of several sectors, such as offshore wind, solar and aquaculture (Buck and Langan, 2017; Maar et al., 2023).

However, offshore structures face harsh environmental conditions that risk the safety of the structures. Thus, mooring systems are essential to ensure the stability of various floating structures, including floating wind turbines, floating solar panels, ships, installation vessels, and aquaculture structures. Especially during extreme events, tensions in single mooring lines are critical to structural safety. Even more critical are snap forces, which can cause early failure of mooring lines (Governo et al., 2023). Snap forces are sudden increases in tensions, which occur after the mooring line becomes temporarily slack.

* Corresponding author at: Faculty of Electrical Engineering, Mathematics and Computer Science, Delft University of Technology, Mekelweg 4, Delft, 2628 CD, The Netherlands.
E-mail address: r.santjer@tudelft.nl (R. Santjer).

https://doi.org/10.1016/j.apor.2025.104809
Received 22 January 2025; Received in revised form 22 May 2025; Accepted 10 October 2025
Available online 16 October 2025

These dynamic snap tensions can exceed static tensions by a multiple, even up to 6-times higher than the static pretension (Guo et al., 2017; Hsu et al., 2017; Miškov et al., 2023).

Research has been done to understand the behaviour and expected tensions in mooring lines under snap loads, using field measurements, numerical simulations and model experiments. Research on field experiments to investigate tensions in mooring line, especially with regard to snap loads, is however limited. Nguyen et al. (2019) measured the tensions in the moorings of an oyster cage along the coast of Maine. The results show that the mooring line tensions correlate with the tide-induced water level variations. Currents have a significant influence at low to mid tidal levels, but not at high tides. Similar results are obtained in Nasyrlayev et al. (2023). A Finite Element Model is used to improve the design of anchors and other structural elements, especially for high-energy regions. The results show that the current magnitude and angle do have a much higher impact on the tensions than those of the waves. Lumped-mass models are extensively used in studies related to aquaculture systems (Hermawan and Furukawa, 2020; Feng et al., 2021), highlighting the complexity of interaction between the environment and the structures. Another Finite Element Model is used by Desiré et al. (2023) to investigate the seabed interaction with mooring lines in complex bathymetries. The model is validated against experimental scale tests for both cases with and without snap loads. Following the analyses of Desiré et al. (2023), experimental tests (Somoano et al., 2024) confirm that bathymetry is another factor influencing the mooring line dynamics. While the quasi-static loads are not impacted by the shape of the bathymetry, the dynamic loads, such as snap loads, are significantly influenced by the slope of the bathymetry.

Experimental investigations at a 1:50 scale, corresponding to a full-scale water depth of 28 m, were conducted to investigate the relationship between snap loads and the damping of mooring lines (Hsu et al., 2019). The results show that snap loads occur more frequently in shallow water settings due to shorter mooring lines and reduced damping. Also, a positive correlation was found between the pretension of a mooring line due to the self-weight with the mooring line damping. The intensity and occurrence rate of snap loads were also investigated in Hsu et al. (2017) through experiments at a 1:50 scale, simulating a floating offshore wind turbine in conditions for very high return periods. The results show that dynamic tensions caused by snap events are 37%–68% higher than non-snapping tension peaks. In addition, these snap loads follow a different exceedance probability distribution than non-snapping peak tensions. A composite Weibull distribution, which has different parameters for lower and higher tension rates, is found to be a good fit to account for snap loads, while the conventional Weibull distribution tends to underestimate how often these extremes occur (Hsu et al., 2017).

Various probabilistic models are applied to assess the reliability and uncertainty of mooring line tensions under stochastic environmental conditions. Regarding peak tensions in mooring lines, Zhao and Dong (2023) identified the Gumbel distribution as the best model to describe them. The study investigates uncertainty of extreme mooring loads of floating systems using environmental contours, which are based on the joint distribution of variables. Li et al. (2016) assesses mooring line fatigue damage using probability density functions (pdf's) for short-term mooring line tension amplitudes, which result from single sea states or short durations, and for long-term amplitudes, which are obtained by integrating the short-term distributions while considering the probability of various sea states. Several different pdf's have been investigated, while the Gamma distribution is a good fit for both short and long-term tension amplitudes, for the latter, the Gamma distribution is extended by a location parameter. Thus, the mooring line tension response is non-Gaussian.

To assess the tensions of mooring lines while considering the relation between variables, Wu et al. (2022) employs conditional probabilities of tensions and Monte-Carlo simulations. The results show that, in case of failure, the tension responses in the remaining mooring lines can be described by the Generalised Extreme Value (GEV) distribution. Conversely, Montes-Iturrizaga and Heredia-Zavoni (2016) evaluates the reliability of mooring lines by investigating the impact of the statistical relationship between the significant wave height and peak spectral period. Therefore, copula functions are used to describe their dependence. The results show that accounting for the dependence structure among environmental variables has a significant impact on the reliability of mooring lines. Modelling the multivariate probability distribution via for example multivariate copula models is determined by Montes-Iturrizaga and Heredia-Zavoni (2016) as an important further step to investigate how environmental variables affect the reliability of floating structures.

Considering the multivariate dependence of variables is crucial for improving the reliability and safety of mooring line systems due to complex environmental conditions and the interactions with the structures. To the authors' knowledge, taking the multivariate dependence of variables into account to assess mooring line tensions due to environmental impacts has not been done before. In this study, the multivariate dependence between hydrodynamic variables and tensions in mooring lines is modelled using a Gaussian copula-based Bayesian Network (GCBN). The nodes of the Bayesian Network represent continuous random variables and the arcs between the nodes describe the (conditional) probabilistic dependence using bivariate Gaussian copulas. Due to the application of copula models, the GCBN has no restrictions on marginal distributions. Thus, the GCBN is a fully probabilistic model accounting for uncertainty. The advantages of a GCBN are many-fold. GCBNs are computationally efficient (see e.g. study Barros et al. (2024) using a GCBN with 879 variables). Their graphical representation of the complex multivariate dependence of a set of variables allows to visually give information about (conditional) independence of variables. Additionally, the model allows for incorporation of prior or new knowledge and thus can be updated given new observations. That is, a GCBN can efficiently and accurately enable inference i.e. providing distributions of variables given observational data as input. This is especially of importance for scenario analysis (e.g. conditionalising on certain variables and analysing the remaining conditional distributions), offering a more comprehensive view of the problem, enabling risk assessment and informed decision-making. The main disadvantage, however, is that the joint dependencies between variables are restricted to the Gaussian copula. This entails that GCBNs cannot reproduce certain asymmetries in the joint distribution such as tail dependence for example.

Regarding the tensions in the mooring lines, this study focuses on extremes of tension rates for two reasons: (1) snap loads, characterised by high tension rates, inducing a strong dynamic response in the floater; (2) operational limitation related to the application of the floater. For example, operation of offshore wind turbines require a constrain on the acceleration of the tower to minimise damage to the blades (Dueñas-Osorio and Basu, 2008). This is similar to another example on aquaculture, where extreme accelerations lead to damages such as mussel fall-off (e.g., Gagnon and Bergeron, 2017; Knysh et al., 2020).

This study takes the mooring line dimensions exemplarily from a seaweed aquaculture structure, specifically a net structure. This reference structure is a pilot designed for offshore conditions in the North Sea, 80 km off the coast, for a water depth of 23 m (Strothotte et al., 2021). Note however, that the methodology as well as the results presented in this study can be transferred to any floating structure, which requires a mooring line.

Environmental data used in this study come from a three-dimensional large-scale hydrodynamic model covering the European Shelf, while a Finite Element (FE) model is used to get observations about tensions within the mooring lines. The mooring line of the aquaculture structure is implemented in the model and adjusted for different water depths. Based on these observations, GCBNs are set up for a few different locations in the south-eastern North Sea. The aim of this study is twofold. The multivariate dependence is analysed

and compared among different locations with different characteristics. This helps to assess which hydrodynamic variables are the main driver for snap loads under different conditions. Secondly, this study shows how the GCBN can be used to help reliability engineering by assessing extreme tension rates conditioned on certain hydrodynamic conditions. Not only are offshore hydrodynamic impacts highly relevant for such structures, but also ecological variables are crucial, particularly in the case of aquaculture. The ecological suitability for the same structure and area was investigated using bivariate copula models in Santjer et al. (2024).

The present study is structured as follows. First, the hydrodynamic model, including the study locations and selected hydrodynamic variables are described in Sections 2.1 and 2.2, while the Finite Element model for mooring lines is described in Section 2.3. Section 3 describes the probabilistic modelling approach, including copula models and copula-based Bayesian networks, in Sections 3.2 and 3.3, respectively, as well as the processing of the numerical tension data (Section 3.4). The results are described in Section 4. First, Bayesian Networks are set up and described in Section 4.1 for the hydrodynamic variables, which output serves as input for the FE mooring line model. The post-processing of the tension data is for one location in the North Sea exemplarily presented in Section 4.2, while the GCBNs consisting of environmental variables and tension rates are described in Section 4.3. Final results analysing extreme tension rates in mooring lines, also under given environmental conditions, are described in Sections 4.4 and 4.5, respectively. Discussion of the results can be found in Section 5 and conclusion of the presented study are drawn in Section 6.

2. Modelling framework and study setup

2.1. 3D hydrodynamic model

Wave and current characteristics at the locations of interest are necessary to determine the tensions in the mooring line of a floating structure for each of these locations. In this study, data is extracted from a large-scale three-dimensional hydrodynamic model called Dutch Continental Shelf Model (DCSM) (Zijl et al., 2023). The DCSM makes use of the D-Flow FM component of the Delft 3D Flexible Mesh Suite (Deltares, 2023) in which the grid is based on a flexible mesh, as the grid resolution is spatially variable. In deep oceanic waters, the grid is coarse with 4 × 4 nm, while it increases towards shallow areas and to coast up to 0.5 × 0.5 nm. Cells that change resolution are connected by triangles. In total, the DCSM consists of 630,000 cells. The domain of the model is between 17°W to 13°E and 43°N to 64°N and thus covers the northwestern European continental Shelf. To account for variations in water depth across the model domain, z-sigma layers are employed for vertical resolution, combining two different types of layers. In the upper 100 m, sigma-layers are utilised, consisting of a fixed number of 20 layers, with varying thickness depending on the water depth. This allows for a high resolution especially in shallow areas. Beneath the sigma-layers, z-layers are employed, which have a fixed depth throughout the domain, while their thickness increases exponentially by a factor of 1.19 towards the deeper layers. Variables describing the current flows are derived from this model with a 10 min resolution, while variables describing the waves are derived from the third general spectral wave model SWAN (simulating waves nearshore (Booij et al., 1999)). SWAN is added on top of the D-Flow FM component and solves shallow-water processes. Data from the models are extracted for 5 years (2013 until 2017).

2.2. Study locations and variable selection

The current study focusses on the south-eastern part of the North Sea, which is well represented by the model domain, which covers the entire northwestern European shelf. Here, 12 spatially distributed locations l are chosen (see Fig. 1, in which the reference location (RefLoc 4) is highlighted). Some of these locations are located close by or within offshore wind farms, others are research platforms or measurement buoys. The close distance to offshore wind farms is relevant, especially in the context of marine multi-use or co-location of several sectors (Buck, 2002; Buck and Langan, 2017; Maar et al., 2023). Furthermore, the selected sites span a variety of depths in this area from approximately 13 m to 45 m (see Table 1) and experience different environmental conditions due to their varying distances from the shore.

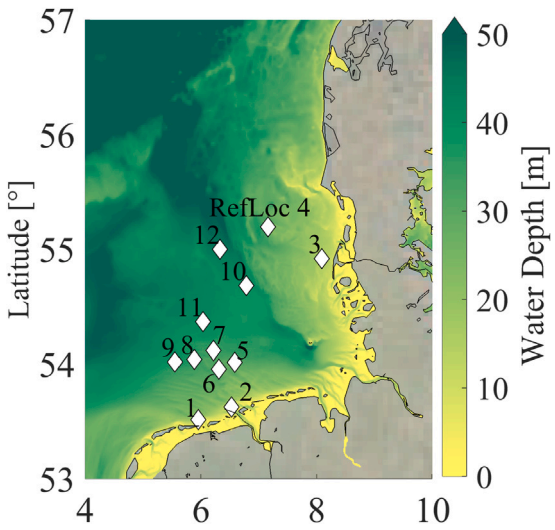

Fig. 1. Map of the south-eastern North Sea, showing 12 study locations (l), with the reference location RefLoc 4 highlighted.

Table 1
Overview of the total water depth (h) in [m] per location l together with depths i of current magnitude [m/s] data throughout the water column, where $d1$ is 1 m above the seabed, while $d5$ is close to the surface.

Location l	Total depth (h)	$d1$	$d2$	$d3$	$d4$	$d5$
1	12.6	1	4	6	9	12
2	14.5	1	4	7	10	14
3	15.0	1	4	7	11	14
4 (RefLoc)	22.8	1	6	11	17	22
5	30.1	1	8	15	22	29
6	30.2	1	8	15	22	29
7	33.6	1	9	17	25	33
8	35.7	1	9	18	26	35
9	38.6	1	10	19	28	38
10	39.2	1	10	20	29	38
11	40.7	1	11	20	30	40
12	44.7	1	12	22	33	44

The main environmental impacts in estimating the tension in the mooring ropes of a (submerged) floating structure are waves and currents, whose characteristics for selected study locations are provided by the DCSM model (see Section 2.1). Specifically, significant wave height, H_S, and peak wave period, T_P, are selected to describe wave characteristics (see Fig. A.11 in Appendix A for an overview of the magnitude of both variables for each location), while for currents, horizontal flows $c_{d,i}$ are considered at different depths i, which are selected according to the water depth per location. The top and bottom 1 m of the water column are excluded from consideration, while the remaining portion of the water column is equally divided into 5 depths. The water depth per location and depth selected for the extraction of the current velocity magnitude is shown in Table 1. Note that the depths are positive as the seabed is the reference level.

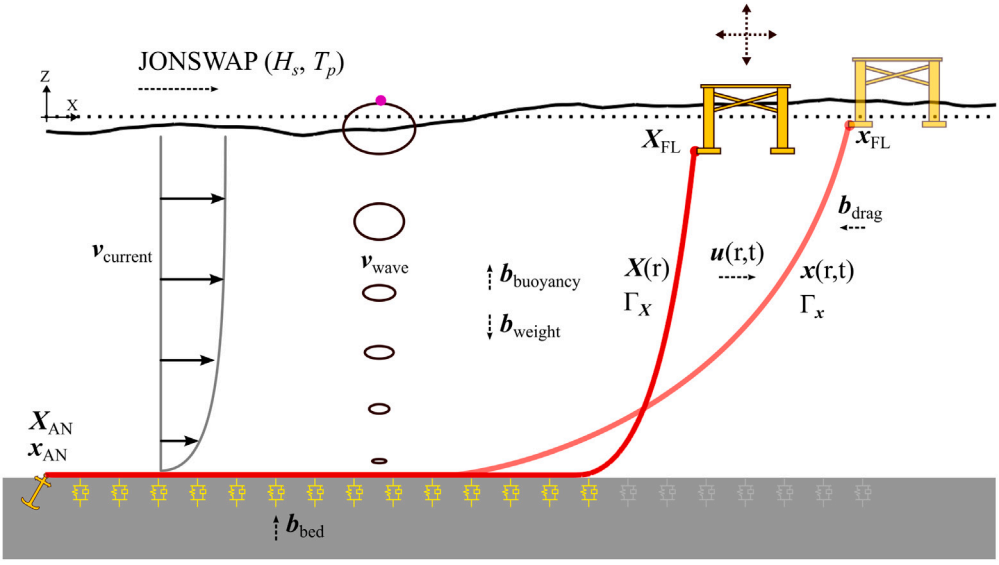

Fig. 2. Schematic of the mooring line, along with the external forces acting on the line.

2.3. Mooring line model

In this study, the mooring line model reported in Agarwal et al. (2025) is employed. This model is specifically developed for flexible cables and incorporates a geometrically non-linear analysis, allowing for large displacements and finite strains. Consequently, it extends beyond the conventional small-strain assumptions. Fig. 2 presents a schematic of the mooring line, along with the external forces considered in this analysis.

The mooring analysis is described in terms of the internal and external forces acting on the line. It is considered to be a curved manifold in 2D XZ space, with $z = 0$ at the mean-sea level. The initial undeformed shape $\Gamma_{\boldsymbol{X}}$ of this manifold is given by a function field $\boldsymbol{X}(r)$. Here r represents a 1D reference domain Ω along the line, and $\boldsymbol{X}(r)$ is its map to the 2D space. For instance, $r = 0$ and $r = L_0$ denote the two end points of the curved manifold $\Gamma_{\boldsymbol{X}}$. The anchor is located at $\boldsymbol{X}(r = 0) = \boldsymbol{X}_{\text{AN}}$, and the fairlead is at $\boldsymbol{X}(r = L_0) = \boldsymbol{X}_{\text{FL}}$. The dynamic deformed shape $\Gamma_{\boldsymbol{x}}$ of the manifold is given by function field $\boldsymbol{x}(r,t)$. The difference between undeformed and the dynamic deformed shape is given by the displacement field $\boldsymbol{x}(r,t) = \boldsymbol{X}(r) + \boldsymbol{u}(r,t)$. The equilibrium of the mooring line is always defined on the dynamically deformed configuration, $\Gamma_{\boldsymbol{x}}$. The equilibrium equation per-unit length is expressed as

$$\rho A\, \ddot{\boldsymbol{u}} - \text{div}_{\Gamma}\, \boldsymbol{\sigma}(\boldsymbol{u}) A - \boldsymbol{b}(\boldsymbol{x}) = 0 \quad \forall \boldsymbol{x} \in \Gamma_{\boldsymbol{x}} \tag{1}$$

Here A is the cross-sectional area, ρ is the material density and $\rho\,\ddot{\boldsymbol{u}}$ represents the inertia of the line. The term $\boldsymbol{\sigma}(\boldsymbol{u})$ is the Cauchy stress tensor and $\text{div}_{\Gamma}\, \boldsymbol{\sigma}(\boldsymbol{u})$ is its *surface divergence*. This term characterises the variation in stress within the line along its curved manifold, effectively capturing the internal material resistance to deformation. Finally, the term $\boldsymbol{b}(\boldsymbol{x})$ represents the external forces acting on the line.

The Cauchy stress tensor is defined based on the Saint Venant–Kirchhoff solids theory. For cables made of material with Young's modulus E and Poisson's ratio ν, the corresponding Lamé constants are $\lambda = 0$ and $\mu = \frac{E}{2(1+\nu)}$. Consequently, the first and second Piola–Kirchhoff stress tensors $\mathbf{K}$, $\mathbf{S}$ on $\Gamma_{\boldsymbol{X}}$ and the Cauchy stress tensor $\boldsymbol{\sigma}$ on $\Gamma_{\boldsymbol{x}}$ are expressed as follows,

$$\boldsymbol{\sigma} = \frac{1}{J} \cdot \mathbf{F}_{\Gamma} \cdot \left(2\mu \cdot \mathbf{E}_{\text{tang}}\right) \cdot \mathbf{F}_{\Gamma}, \tag{2}$$

where $\mathbf{F}_{\Gamma}$ is the *surface deformation gradient*, and $\mathbf{E}_{\text{tang}}$ tangential Cauchy–Green strain tensor. For further details regarding the structural model, see Agarwal et al. (2025).

The external force acting on the line include self weight, buoyancy of the surrounding fluid, drag due to relative motion against the fluid and the effect due to the sea-bed. Since the external forces are a function of the position on the line, the external forces are defined per-unit length. Self weight of the line is simply given by

$$\boldsymbol{b}_{\text{weight}}(\boldsymbol{x}) = -\rho\, A\, g\, \hat{k}, \tag{3}$$

where g is the acceleration due to gravity and $\hat{k}$ is a unit vector along the vertical axis. The force of buoyancy is given by the weight of water displaced by the line,

$$\boldsymbol{b}_{\text{buoyancy}}(\boldsymbol{x}) = \rho_{\text{water}}\, A_{\text{disp}}\, g\, \hat{k}, \tag{4}$$

where ρ_{water} is the density of water, A_{disp} is the displaced volume per unit-length of the line.

The effect of the sea-bed is implemented using a damped spring, which is activated only for the portion of the line in contact with the sea-bed, i.e.

$$\boldsymbol{b}_{\text{bed}}(\boldsymbol{x}) = \begin{cases} -k_b \left(z - z_{\text{bed}}\right) \hat{k} - c_b \dot{z}\, \hat{k} & \text{if } z \le z_{\text{bed}} \\ 0 & \text{if } z > z_{\text{bed}} \end{cases} \tag{5}$$

The drag forcing on the line is due to three components,(1) self drag, (2) action of the current, and (3) wave action. If $\boldsymbol{v}_{\text{wave}}(\boldsymbol{x})$ is the local velocity of the wave and $\boldsymbol{v}_{\text{current}}(\boldsymbol{x})$ the local current velocity, then the drag force on the line is given by

$$\boldsymbol{b}_{\text{drag},n}(\boldsymbol{x}) = \frac{1}{2} \rho_{\text{water}}\, C_{d,n}\, \boldsymbol{v}_{r,n}(\boldsymbol{x}) |\boldsymbol{v}_{r,n}(\boldsymbol{x})| \tag{6}$$

$$\boldsymbol{b}_{\text{drag},t}(\boldsymbol{x}) = \frac{1}{2} \rho_{\text{water}}\, C_{d,t}\, \boldsymbol{v}_{r,t}(\boldsymbol{x}) |\boldsymbol{v}_{r,t}(\boldsymbol{x})| \tag{7}$$

$$\text{where } \boldsymbol{v}_r(\boldsymbol{x}) = \boldsymbol{v}_{\text{wave}}(\boldsymbol{x}) + \boldsymbol{v}_{\text{current}}(\boldsymbol{x}) - \dot{\boldsymbol{u}}(\boldsymbol{x}) \tag{8}$$

$$\boldsymbol{v}_{r,t}(\boldsymbol{x}) = \left(\boldsymbol{v}_r(\boldsymbol{x}) \cdot \hat{t}(\boldsymbol{x})\right) \hat{t}(\boldsymbol{x}) \tag{9}$$

$$\boldsymbol{v}_{r,n}(\boldsymbol{x}) = \boldsymbol{v}_r(\boldsymbol{x}) - \boldsymbol{v}_{r,t}(\boldsymbol{x}) \tag{10}$$

In the present analysis, it is not accounted for the influence of added mass and added damping of the mooring line. This is based on the findings in Hall and Goupee (2015), which demonstrate the limited impact of added mass on the overall system response.

The definition of the boundary value problem is completed by specifying the boundary conditions at the two ends of the mooring line. A Dirichlet-type boundary condition is applied, with the anchor fixed at $\boldsymbol{u}(r = 0, t) = \boldsymbol{u}_{\text{AN}} = [0.0, 0.0]^T$, and a prescribed motion for the fairlead $\boldsymbol{u}(r = L_0, t) = \boldsymbol{u}_{\text{FL}}(t)$.

Table 2
Properties of mooring line.

Property		Value
Diameter		0.068 m
Cross-sectional area	A	0.003619 m^2
Mass per unit length	ρA	28.23 kg m^{-1}
Axial stiffness	EA	232.7 MN
Unstretched length	L_0	75 m or 105 m
Normal drag coefficient	$C_{d,n}$	2.6
Axial drag coefficient	$C_{d,t}$	1.4
Sea-bed stiffness	k_b	3×10^6 Pa m^{-1}
Sea-bed damping	c_b	3×10^5 Pa s m^{-1}

Table 3
Position of the anchor and the fairlead for all locations.

Location l	Total depth (h) m	L_0 m	L_{susp} m	$\boldsymbol{X}_{AN}$ m	$\boldsymbol{X}_{FL}$ m	k_{xx} N m^{-1}
1	12.6	75	10.72	$[0.0, -12.6]^T$	$[67.7, -3.0]^T$	218
2	14.5	75	12.79	$[0.0, -14.5]^T$	$[66.3, -3.0]^T$	218
3	15.0	75	13.40	$[0.0, -15.0]^T$	$[65.9, -3.0]^T$	218
4 (RefLoc)	22.8	75	22.14	$[0.0, -22.8]^T$	$[60.0, -3.0]^T$	218
5	30.1	75	30.27	$[0.0, -30.1]^T$	$[54.5, -3.0]^T$	218
6	30.2	75	30.36	$[0.0, -30.2]^T$	$[54.4, -3.0]^T$	218
7	33.6	75	34.16	$[0.0, -33.6]^T$	$[51.8, -3.0]^T$	218
8	35.7	75	36.46	$[0.0, -35.7]^T$	$[50.2, -3.0]^T$	218
9	38.6	105	39.78	$[0.0, -38.6]^T$	$[78.0, -3.0]^T$	218
10	39.2	105	40.43	$[0.0, -39.2]^T$	$[77.6, -3.0]^T$	218
11	40.7	105	42.15	$[0.0, -40.7]^T$	$[76.4, -3.0]^T$	218
12	44.7	105	46.54	$[0.0, -44.7]^T$	$[73.4, -3.0]^T$	218

The governing equations are numerically solved using the finite-element method. The definition of surface gradients along curved manifolds is done using the *Tangential Differential Calculus* approach presented in Fries and Schöllhammer (2020). The formulation of the variational problem is done using the standard Galerkin approach. The reference domain Ω is discretised using linear Lagrangian elements, while the time-stepping is implemented using the implicit Generalised-α method (Chung and Hulbert, 1993). A detailed description of the mooring line model is given in Agarwal et al. (2025). It also presents rigorous investigation of numerical convergence properties, validation of the model for conventional chain mooring lines and a detailed study of non-linear hardening of taut mooring lines.

The properties of the line modelled in this study are listed in Table 2. These properties represent an engineer design for a steel-wire type mooring line. However, the approach for the mooring model and the probability analysis can be directly applied to chain, synthetic or composite mooring lines.

The initial shape $\Gamma_{\boldsymbol{X}}$ of the mooring line is defined by solving the catenary equation. The anchor is located at $\boldsymbol{X}_{AN} = [0, -h]^T$, where h represents the total water depth, as detailed in Table 1. The fairlead is positioned at $\boldsymbol{X}_{FL}$, with its coordinates listed in Table 3. For each location, the fairlead is placed 3 m below the mean sea level. The horizontal position of the fairlead is determined to ensure consistent surge restoring stiffness k_{xx} of the mooring line across all locations. Table 3 presents the surge restoring stiffness values for each mooring line. To calculate this surge restoring stiffness, we evaluate the horizontal restoring force at the fairlead for two displaced positions: $\boldsymbol{X}_{FL}+[0.01h, 0]^T$, yielding $\boldsymbol{f}^+_{FL} = [f^+_x, f^+_z]$, and $\boldsymbol{X}_{FL}-[0.01h, 0]^T$, yielding $\boldsymbol{f}^-_{FL} = [f^-_x, f^-_z]$, where h denotes the water depth. The surge restoring stiffness is then computed as $k_{xx} = \frac{f^+_x - f^-_x}{2\times 0.01h}$.

Table 3 also includes the calculated length of the suspended portion of the line, L_{susp}, in the initial configuration. It is important to note that the total initial length of the line, L_0, is selected solely to ensure that the line does not become taut or fully suspended during the tested sea states. Consequently, for locations 10–12, which correspond to greater water depths, the total line length is increased from 75 m to 105 m to prevent the line from becoming taut or fully suspended.

The loads on the line are determined by the environmental conditions. The velocity profiles for the current and wave are the key parameters controlled in this study. The current velocity profile along the depth is specified at five discrete depths listed in Table 1, $\boldsymbol{v}_{current}(z = -di) = c_{di}$, and subsequently interpolated across the entire depth using the piecewise cubic Hermite interpolating polynomial (PCHIP) method. The wave environment is defined using a JONSWAP spectrum with the values of significant wave height (H_s) and peak time-period (T_p). The wave particle velocity $\boldsymbol{v}_{wave}$ is then calculated by first obtaining a wave time-series via an inverse Fourier transform (IFFT) of the input spectrum, followed by application of the linear wave theory. The direction of propagation for the wave and the current are assumed to be along the mooring line, since this represents the extreme scenario for external loads acting on the line. The bed properties used in this study are also listed in Table 2.

The final component of the problem definition is the motion of the fairlead, $\boldsymbol{u}_{FL}$. The motion of the fairlead is governed by the dynamics of the floating body to which the mooring line is attached. In this analysis, we assume the mooring line is connected to a weightless buoy. Therefore, the characteristics of the floater, the forces acting on it, and, as a result, its dynamic response are not considered in the scope of this analysis. Consequently, the fairlead is assumed to follow the motion of the local wave particle. This assumption is made for two key reasons: (1) it represents the most extreme scenario for the motion of the floater; and (2) it is easily replicable in numerical models or through simple experimental setups, such as those described in Bergdahl et al. (2016), without the typical challenges associated with scaled physical modelling of floaters. Accordingly, the motion of the fairlead is prescribed using an inverse fast Fourier transform (IFFT) and linear wave theory applied to the input JONSWAP spectrum, with the wave particle position calculated around $\boldsymbol{X}_{FL}$.

We would like to note that the current approach can be readily extended to include floater dynamics. If floater dynamics are incorporated, it would then be necessary to account for the second-order forcing acting on the floater within the analysis. We would like to highlight that the second-order forcing on the mooring line, resulting from wave and current-induced drag, is already included in the present study via Eqs. (6)–(7). Incorporating floater properties would make the resulting Bayesian network specific to those floater properties. Therefore, to address a more general case, it would be necessary to consider a range of floater characteristics and include them as inputs to the Bayesian network. While this is beyond the scope of the current manuscript, we intend to explore this direction in future work.

3. Modelling approach

In this section, the methodology is described. An overview of the detailed methodology is presented in Fig. 3.

First, data is extracted from the DCSM hydrodynamic model for the months September to April for each location l of interest. This winter period is chosen, as this is the main growth period of the species Saccharina latissima, whose cultivation structure at RefLoc 4 serves as a foundational basis for this study. The daily maxima of the significant wave height, H_S, are selected together with the corresponding peak wave period, T_P. This is because wave heights have a greater influence on the mooring line tensions than current flows v_{di}. The maximum of current flows v_{di}, within a time window of ±4 h around the daily maximum of the wave height, at the depths describes above are selected as concomitants.

In the next step, Spearman's rank correlations (Spearman, 1987) between the variable pairs per location in the North Sea are analysed. Based on the underlying physics and correlation matrices, structures of individual Bayesian Networks (BNs) are set up, denoted as $BN_{h,l}$. Therefore, two goodness-of-fit measures are applied, the d-calibration score and the Cramér–von Mises method (CvM). Both, the BNs and goodness-of-fit measures, are further described in Section 3.3. From

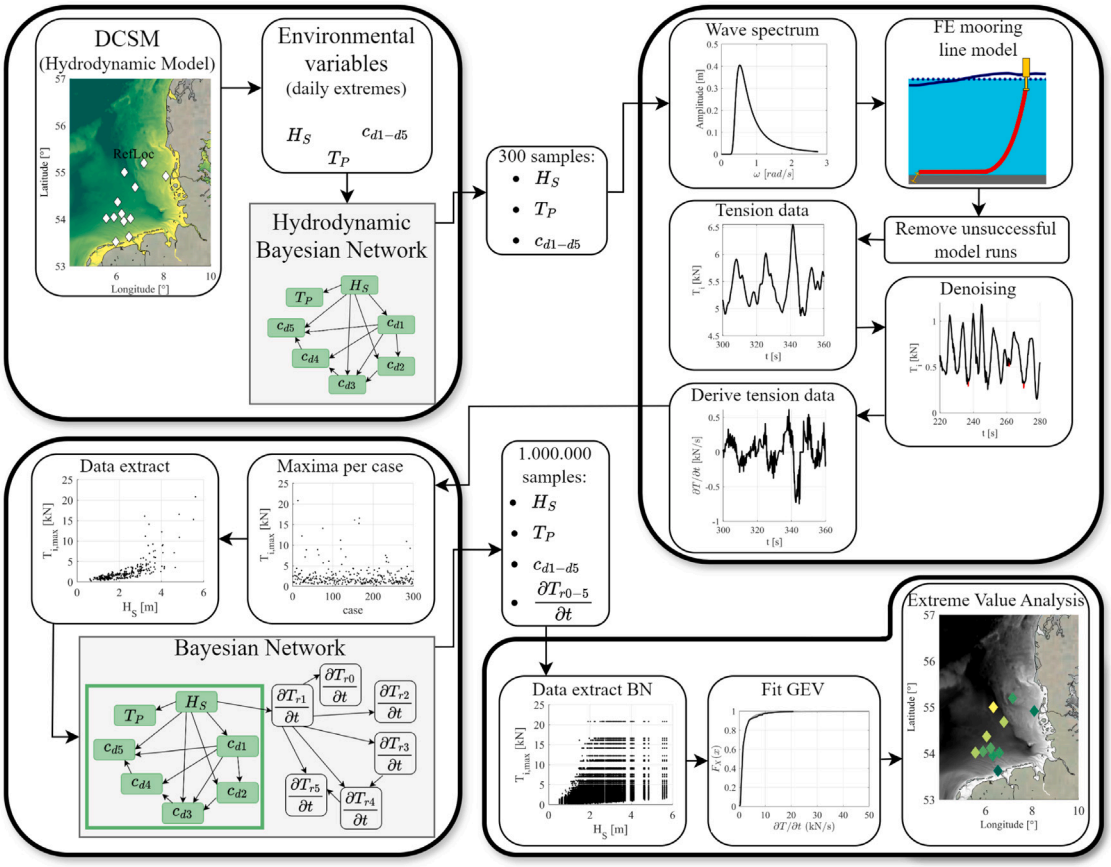

Fig. 3. Detailed framework of the methodology applied in this study.

each $BN_{h,l}$, $n = 300$ samples are drawn. Wave spectra per sample set are generated and, along with steady current flow magnitudes, serve as input for the finite-element model for flexible mooring lines.

The flexible mooring line model produces time series data of tensions at the anchor, T_{r0}, fairlead, T_{r5}, and four intermediate rope positions p, T_{r1-4}. In certain scenarios, the numerical model exhibited poor convergence, particularly in cases involving line folding or the presence of compression. Additionally, the tension time-series contains occasional instances of noise introduced by the spring–damper seabed. The handling of these issues is summarised in Section 3.4. The tension time-series are then derived and maximum tension rates, $\frac{\partial T_{r,p}}{\partial t}$, at the same rope positions p are selected.

For each location l in the North Sea, extended BNs are established, $BN_{ht,l}$, incorporating hydrodynamic data from $BN_{h,l}$, which served as input for the flexible mooring line model, and maxima of tension rate data at different rope locations, p, $\frac{\partial T_{r,p}}{\partial t}$. These $BN_{ht,l}$ are also assessed via two goodness-of-fit measures and generate a sample set of $n = 1.000.000$ samples per location l. The structures of $BN_{ht,l}$ provide further understanding of the underlying relationships among variables and their spatial differences.

Finally, the tension rate data $\frac{\partial T_{r,p}}{\partial t}$ generated by $BN_{ht,l}$ are fitted to a Generalised Extreme Value (GEV) distribution, to obtain values corresponding to certain probabilities for each study location.

3.1. Spearman's rank correlation coefficient

Between each pair of variables, Spearman's rank correlation coefficient, ρ, is calculated (Spearman, 1987). This acts as a foundation for the dependence analysis and the structure of the Bayesian Network for each location. Spearman's rank correlation coefficient ρ is Pearson's correlation coefficient (Pearson and Galton, 1895) computed with the ranks of each variable. It assesses the degree of monotonic dependence between the random variables and is given by

$$\rho = \frac{Cov[R(X), R(Y)]}{\sigma_{R(X)}\sigma_{R(Y)}} \tag{11}$$

where the covariance of the ranked variates of X and Y is denoted $Cov[R(X), R(Y)]$, and $\sigma_{R(X)}$ and $\sigma_{R(Y)}$ are their standard deviations. $\rho \in [-1, 1]$, where $\rho = 1$ and -1 denote perfect (monotonic) positive and negative correlation, respectively. The significance of observed correlations is assessed by computing p-values using the student-t distribution (Zar, 1972):

$$t = \rho \sqrt{\frac{n-2}{1-\rho^2}} \tag{12}$$

where n represents the sample size or degrees of freedom. The p-value is defined as the combined area in both tails of the student-t distribution. The p-value per tail is obtained from the cumulative distribution function of the student-t distribution, evaluated at the t-score from (12) with $(n-2)$ degrees of freedom. A rank correlation is statistically significant if the p-value falls below the significance level of $\alpha = 0.05$.

3.2. Bivariate copulas

Copula models are a popular approach to model the dependence structure between random variables, independent from their marginal distributions. Any joint multivariate distribution can be described in terms of a set of one-dimensional univariate marginal distributions in [0,1] and a copula that models the dependence between the random variables (Sklar, 1959). For the bivariate case, let $H(x, y)$ for $(x, y) \in \mathbb{R}^2$ be a joint distribution with univariate marginals $F(x)$ and $G(y)$, then there exists a copula C in the unit square $I^2 = ([0, 1] \times [0, 1])$:

$$H(x, y) = C(F(x), G(y)) \tag{13}$$

Eq. (13) is satisfied for all $(x, y) \in \mathbb{R}^2$ (Nelsen, 2006; Genest and Favre, 2007; Joe, 2015).

3.3. Gaussian copula-based Bayesian Network

A Bayesian Network is a probabilistic graphical model to represent high-dimensional and complex dependence structures (Hanea et al., 2006). Bayesian Networks are directed acyclic graphs (DAG), representing the joint distribution of a set of variables. Each node represents a random variable, while the arcs between the nodes describe (conditional) probabilistic dependence between the variables. The predecessor and successor of a node are called parent and child nodes, respectively. In this study, this dependence is described via one-parameter conditional copulas, which are parameterised by Spearman's rank correlation coefficient ρ (Hanea et al., 2015). Here, the Gaussian copula is selected for its computational efficiency, enabling fast inference when handling large and complex problems. Thus, the dependence structure of the variable set is described by a multivariate normal distribution. Note, however, that for a copula-based Bayesian Network, any other one-parameter copula could be used to describe the joint dependence of variables. Each node represents a random variable described by its empirical distribution function. Absence of arcs between nodes indicates conditional independence between two variables (Hanea et al., 2015). The joint probability density function (pdf) of a Gaussian copula-based Bayesian Network (GCBN) with m variables can be described as:

$$f_{1,\dots,m}(x_1, \dots, x_m) = f_1(x_1) \prod_{v=2}^{m} f_{v|Pa(v)}(x_v|x_{Pa(v)}) \tag{14}$$

where the joint density of m variables is denoted as $f_{1,\dots,m}$, the marginal densities are denoted by f_v and the conditional densities are denoted by $f_{v|\cdot}$. Note that each node v represents a variable X_v, while the parent nodes of v form the set $Pa(v)$ (Hanea et al., 2015).

To assess the goodness of fit of the Gaussian copula models per variable pair, the Cramér–von Mises (CvM) statistic S_n is used (Genest et al., 2009). The sum of squared differences between the empirical joint cumulative distribution function (cdf) and the joint cdf of the parametric copula model is determined. S_n, the CvM test statistic, for a sample length of n is determined as:

$$S_n(\boldsymbol{u}) = n \sum_{|n|} \left\{ C_n(\boldsymbol{u}) - C_{\hat{\theta}_n}(\boldsymbol{u}) \right\}^2 \quad , \boldsymbol{u} \in [0,1]^2 \tag{15}$$

Here, $C_n(\boldsymbol{u}) = \frac{1}{n} \sum_{i=1}^{n} 1\left(U_i \le \boldsymbol{u}\right)$ is the empirical copula and $C_{\hat{\theta}_n}(\boldsymbol{u})$ is the parametric copula with the parameter $\hat{\theta}_n$ estimated from the sample. The lower $S_n(\mathbf{u})$ for the Gaussian copula compared to other copula models, the better the Gaussian copula-based Bayesian Network (GCBN) captures the joint dependence among variable pairs. Another goodness-of-fit measure, known as d-calibration score (Morales-Nápoles et al., 2014), is applied. The dissimilitude between two correlation matrices is determined via the Hellinger distance, where a score of 0 indicates that the correlation matrices differ element-wise, while a score of 1 signifies identical matrices. The d-calibration score, however, is sensitive to the sample size. For more information, the reader is referred to Morales-Nápoles et al. (2014).

In this study, the open-source Python library BANSHEE, version 1.3, is used for implementing GCBNs and for the calculation of the goodness-of-fit measures d-calibration score and CvM statistics (see Paprotny et al. (2020), Koot et al. (2023) and for the MATLAB implementation see Mendoza-Lugo and Morales-Nápoles (2023)).

3.4. Processing of numerical tension data

The finite-element model for flexible mooring lines, described in Section 2.3 provides time series of tension data in the mooring line for different positions p in the rope, while the tension close to the anchor, T_{r0}, fairlead, T_{r5}, and 4 intermediate depths, T_{r1-4}, are chosen for the analysis. These time series have a resolution of 0.1 s and a duration of 23 min, of which the first 3 min are used as ramp-up time and are disregarded from the analysis. If the finite-element model fails to converge at a given time-step due to unphysical folding or compressive forces, the corresponding data point, along with 1 second before and after, are removed from the analysis in post. If a model run does not converge for more than 5 times, it is disregarded from the analysis. As a result, each location l in the North Sea has between 286 and 300 cases. Location 1, which has the shallowest water depth among all locations, was excluded from the analysis. In this location, the mooring line frequently became slack, primarily because the selected line properties and the catenary configuration were unsuitable for such shallow water depths. Ideally, a multi-segment mooring system incorporating a buoy would be more appropriate for this location to reduce the required line length. A single-segment catenary system alone would necessitate an impractically long line.

Before transforming the tension data, $T_{r,p}$, to the relevant tension rates, $\frac{\partial T_{r,p}}{\partial t}$, outliers are removed from the time series. These outliers primarily result from the damped-spring implementation of the seabed. The spring and damper coefficients for the seabed, listed in Table 2, were selected to function effectively in most cases. However, in certain instances, they may be slightly stiffer or more compliant than necessary, leading to occasional outlier values. An outlier is detected if its value exceeds three-times the moving-median of the tension time series. Spikes are removed only if they occur for a single time step. This ensures that potentially realistic snap loads, which typically persist over multiple time steps, are not erroneously filtered out. To properly analyse snap loads, which are characterised by high tension rates, $\frac{\partial T_{r,p}}{\partial t}$, they are in a next step obtained by applying the second order central difference approximation to the tension data $T_{r,p}$. The processing of the tension rate is performed in post-processing for two reasons: (1) it enables the filtering of outliers and irregularities in the tension time series, providing a more informed calculation of the tension rate, and (2) the second-order accurate central difference approach is more general and does not require exporting data from intermediate steps.

In a next step, extremes of tension rates, $\frac{\partial T_{r,p}}{\partial t}$, are selected for further analysis. Therefore, two approaches are compared: block maxima (BM) and peaks-over-threshold (POT). According to the Fisher-Tippett theorem (Fisher and Tippett, 1928), the probability distribution of a sample of the maxima per block (here, a block is defined as a case of 20 min simulation time) converges to generalised extreme value (GEV) distributions. While, according to Pickands' theorem (Pickands, 1975), the probability distribution of a sample of peaks-over-threshold converges to generalised Pareto distributions (GPD). There is equivalence between these distributions, which have the same shape parameter. Thus, the GPD is compared with the GEV for the tension rates at the anchor, $\frac{\partial T_{r0}}{\partial t}$, for the reference location (RefLoc) 4, as this position p in the rope exhibits most extremes. To fit the GPD, a threshold is defined via an analysis of the stability of parameters of the GPD for different tension rate percentiles. The 90th percentile is found to be a proper threshold. Design values for the GEV and GPD are calculated and found to be close to each other. Because of this and because the data used in this study is already available as independent blocks in a sufficiently high amount, the block maxima are chosen to obtain extreme tension rates for further analysis. Additionally, the GEV is also recommended by Xu and Guedes Soares (2021), who analysed different distribution models for extreme mooring tensions. However, mixture distribution models might offer a better fit under certain conditions (see also Xu et al. (2022)).

4. Results

4.1. Hydrodynamic Gaussian copula-based Bayesian networks

Before generating tension data with the FE mooring line model described in Section 2.3, hydrodynamic input data are required for the

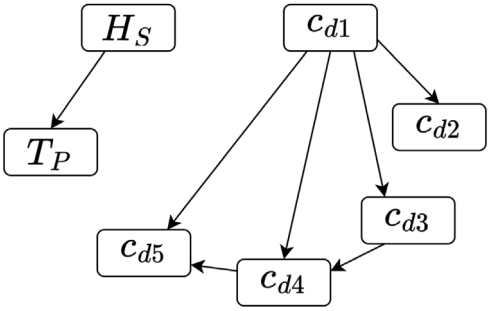

Fig. 4. Underlying structure of GCBNs applicable to all locations with respect to hydrodynamic variables. For each location l, certain arcs are added to account for location-specific dependence structures.

model. Therefore, the daily extremes from the DCSM model are used to set up Gaussian copula-based Bayesian Networks (GCBNs), which generate a set of $n = 300$ data. This is done as the selected data from the DCSM could under-represent extremes, as it only spans five years and thus may not capture rare but critical conditions. Thus, the GCBNs generate data whose dependence is described by the Gaussian copula. These data, account for diverse conditions, while accounting for the underlying dependence structure of the hydrodynamic variables.

In this section, the structures of the GCBNs of the hydrodynamic data for each location l are described, denoted as $BN_{h,l}$. Therefore, seven variables are considered, as described above: significant wave height H_S, peak wave period T_P and current magnitudes $c_{d,i}$ at five different depths i throughout the water column (see Table 1). Fig. B.12 in Appendix B presents the hydrodynamic data from the DCSM for RefLoc 4, which serves as input for $BN_{h,4}$. The data has been transformed to uniform [0,1] to facilitate its use in the copula models (see Section 3.2). The uniform marginal distributions are shown on the diagonal. The pairwise Spearman rank correlation coefficients, ρ, are displayed on the upper-right part of Fig. B.12, while the scatter plots in the lower-left section of the figure show the relationship between variables. Visually, some asymmetries in the bivariate pairs are observed. In order to further investigate this observation, we use the CvM statistic, which is described in Section 3.3. According to CvM, the dependence structure of the variable pair of H_S and T_P is best captured by the symmetric Frank copula, while for other variable pairs, the Gaussian copula is generally the most suitable fit; however, there are instances where the Frank or asymmetric Gumbel copulas provide comparable fits. Given that the results of the CvM statistic predominantly indicate that the symmetric Gaussian or Frank copulas provide the best fit, the GCBN (see Section 3.3) is deemed an acceptable method for modelling the dependence among hydrodynamic variables.

Fig. 4 shows the underlying structure, which is valid for all 12 locations l in the south-eastern North Sea (see Fig. 1). For each arc, the correlation between the variable pair is $r \geq 0.2$, while the significance level is below the threshold ($\alpha \leq 0.05$). In general, there is a strong correlation between the wave variables H_S and T_P. Regarding the current variables, the current magnitude near the seabed, denoted c_{d1}, has arcs to the current magnitudes throughout the water column, c_{d2-5}. To ensure that the $BN_{h,l}$ adequately captures the correlation matrix among current magnitudes, additional arcs between c_{d3} and c_{d4}, as well as between c_{d4} and c_{d5} are necessary. In addition, the northern locations 3, 4 and 12 (see Fig. 1) require an arc between c_{d2} and c_{d3}, despite their different water depths. The single $BN_{h,l}$ structures per location l are shown in Fig. C.13 in Appendix C, marked in green.

Further differences in the structures of $BN_{h,l}$ among locations are observed on how the wave variables are connected with the current magnitudes. An arc consistently connects H_S with the current magnitude near the seabed c_{d1} or the current magnitude near the surface c_{d5}, or sometimes both. Specifically, the following patterns are observed.

For all locations l in the area of interest, except locations 1 and 3, an arc connects H_S with the current component with the highest correlation and $\alpha \leq 0.05$, which is mostly c_{d5}, as this is the current close to the surface. Different from that, an arc between H_S and c_{d1} is added for all locations except for location 2 and 11 (shown in Figs. C.13(b) and (i)). As shown in Fig. 4, c_{d1} points to the other current variables c_{d2-5}.

In general, the following procedure is observed among the offshore locations 4 until 12, while the GCBN structure of location 11, $BN_{h,11}$, requires the least amount of arcs (Fig. C.13(i)).

- Adding an arc between H_S and c_{d1} leads to the GCBN structures of location 5, 6 and 7, $BN_{h,5-7}$, (see Fig. C.13(e)).
- The structure of $BN_{h,5-7}$ results in the GCBN structure of location 8 and 9, $BN_{h,8-9}$, by adding another arc between H_S and c_{d3} (see Figs. C.13(f) and (g)).
- The addition of an arc between H_S and c_{d2} leads to the structure of location 10, $BN_{h,10}$, (see Fig. C.13(h)).
- Another additional arc between c_{d2} and c_{d3} represents the structure of the GCBN for location 4, $BN_{h,4}$, and 12, $BN_{h,12}$, (see Figs. C.13(d) and (j)).

For the nearshore locations, certain arcs of $BN_{h,4}$ and $BN_{h,12}$ can be removed to get a satisfactory fit of the correlation matrix of the GCBN for these locations.

- Based $BN_{h,4}$ and $BN_{h,12}$, removing arcs between H_S and c_{d3} and H_S and c_{d5} results in $BN_{h,3}$.
- Additionally, $BN_{h,1}$ results from $BN_{h,11}$ by removing an arc between H_S and c_{d5} and adding an arc between H_S and c_{d1}, which is necessary, despite the slightly lower correlation compared to the correlation between H_S and c_{d5}. A connection between these variables degrades the fit, possibly because c_{d1} instead of c_{d5} points to the other current variables.
- $BN_{h,2}$ also builds on the structure of $BN_{h,11}$ by removing an arc between H_S and c_{d1}.

Summarising, it can be observed that the smaller the distance of a location to the shore and the more it is affected by strong (tidal) currents (e.g. between islands or close to an estuary, see locations 1 to 3, 5 to 8 and 11), the fewer arcs are required compared to locations further offshore (e.g. locations 4, 10 and 12).

4.2. Methodological application on tension data exemplified by the RefLoc 4

In this section, the described methodology in Section 3.4 regarding the processing of the tension data, T_{r0-5}, of the FE model is applied and presented for the RefLoc 4 as an example. Similar type of analyses may be performed on other locations.

4.2.1. Denoising of tension data

First, the denoising process of the tension data $T_{r,p}$ described in Section 3.4 is demonstrated. Although all tension data time-series throughout the mooring line undergo the described denoising process, the anchor rope position is selected here to showcase the process. This is, because for the tension data at the anchor, T_{r0}, unrealistic spikes due to numerical errors are most frequent and intense, compared to other positions p along the rope at different depths. Fig. 5*(a)* shows the denoised time-series of T_{r0} for the shallow location 2 under moderate conditions ($H_S = 3.1$ m, $T_P = 8.1$ s) and *(b)* shows the denoised time-series of T_{r0} under more intense conditions for the RefLoc 4 ($H_S = 3.6$ m, $T_P = 11.0$ s). Both time-series have a duration of 20 min.

Fig. 5*(c)* and *(d)* demonstrate the difference of the raw time-series (in red) and the denoised time-series (in black). *(c)* shows a segment of *(a)*, and *(d)* shows a segment of *(b)*, each for 50 s respectively. The denoised time-series are obtained by detecting and removing the outliers, which are no longer than one timestep, i.e. 0.1 s, and interpolating linearly among them. This is necessary since the tension rates,

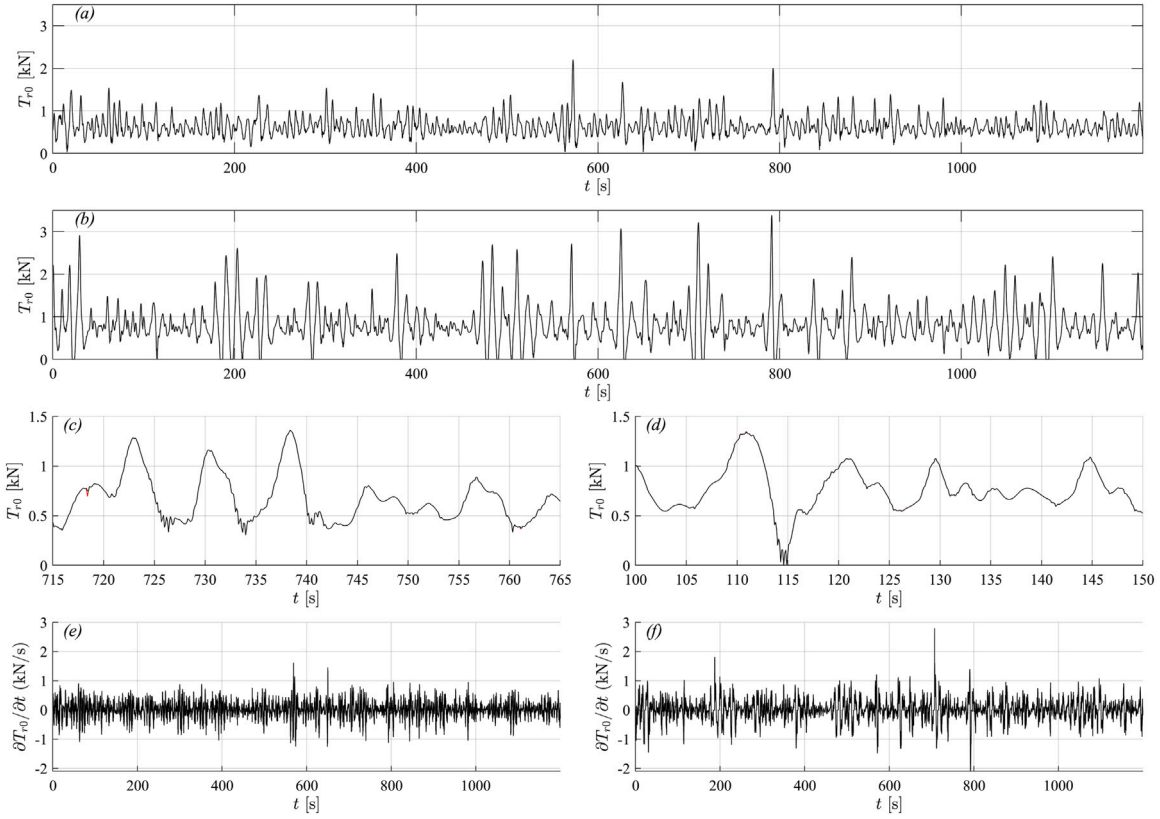

Fig. 5. Anchor data visualisation: (*a*) Denoised tension data for shallow location 2 under moderate conditions (H_S = 3.1 m, T_P = 8.1 s); (*b*) Denoised tension data for RefLoc 4 under storm conditions (H_S = 3.6, T_P = 11.0); (*c*) Close-up view of raw versus denoised tension data for shallow location 2 under the same conditions as in (*a*); (*d*) Close-up view of raw versus denoised tension data for RefLoc 4 under the same conditions as in (*b*); (*e*) Tension rate data for shallow location 2 under the same conditions as in (*a*); (*f*) Tension rate data for the RefLoc 4 under the same conditions as in (*b*).

$\frac{\partial T_{r0-5}}{\partial t}$, for later analysis are derived from the time-series of T_{r0-5} via the second order central difference approximation. Thus, peaks in T_{r0-5}, which stem unphysically from the seabed spring–damper system, lead to unrealistically high tension rates.

The obtained tension rates, $\frac{\partial T_{r,p}}{\partial t}$, for a shallow location in Fig. 5*(a)* are shown in *(e)*, while the tension rates for the RefLoc 4 from *(b)* are displayed in *(f)*. The maxima of the time-series of $\frac{\partial T_{r0-5}}{\partial t}$ are selected per case for each location l in the North Sea.

4.2.2. Analysis of variables in physical units

These extreme tension rates, along with the hydrodynamic data, which was used as input for the FE model, are subsequently utilised to set up extended GCBNs. Here, the data for the RefLoc 4 is presented in Fig. 6. On the diagonal, the empirical distributions are shown as histograms. On the lower-left part of the figure, the scatter plots per variable pair are presented, which allow for a comparison of pairwise relationships. Among the current magnitudes, c_{di} at different depths i, strong correlations are visible, especially among current magnitudes that are closely aligned depth-wise. A similar, even stronger pattern can be observed for the tension rates, $\frac{\partial T_{ri}}{\partial t}$, at different positions in the mooring line. On the top-right part of Fig. 6, Spearman's rank correlation coefficients ρ are shown, which confirm these observations. These correlations are further analysed in Section 4.2.3. As described above, the denoising process aims to remove unrealistic spikes in the data. However, occasionally, more extreme values tend to occur at greater depths. Less extreme tension rates in upper rope positions, such as at the fairlead, $\frac{\partial T_{r5}}{\partial t}$, are due to the weight of the mooring line, which might dampen sudden movements and reduces extreme tension rates in these rope positions.

4.2.3. Analysis of variables in $[0,1]^2$

In a next step, the 13 variables are transformed into a uniform distribution on the interval $(0, 1)$. This is important as the applied GCBN is based on using Gaussian copulas (see Section 3.3), which operate in this interval.

Fig. 7 shows the ranked variables for the RefLoc 4 (FINO3) as pairwise scatter plots on the lower-left part, together with the one-dimensional uniform margins on the diagonal and their density contour plots on the top-right part of the figure. This allows one to better see the above described correlations between variables independent from their margins, different from Fig. 6, which shows the variables in their physical units. Here, a high correlation between the significant wave height H_S and the tension rates, is visible. This is also evident in the corresponding density plot, where the contours have a narrow and symmetric shape. This indicates that H_S is the main driver for the tension rates in this case, as the correlations between T_P or $c_{d,i}$ with tension rates are significantly lower.

4.3. Bayesian networks of hydrodynamic variables and tension rates

The GCBN structures of the hydrodynamic input variables described in Section 4.1 are extended by the derivatives of the tensions, $\frac{\partial T_{r,p}}{\partial t}$, at different positions p in the mooring line. The structures of the GCBNs for each location l in the North Sea, denoted $BN_{ht,l}$, can be found in Appendix C.

For each location l, different structures have been compared and assessed, to identify the one that best represents the dependence structure of the empirical data, hydrodynamic data from the DCSM and maxima of tension rates, while aiming to minimise complexity by keeping the number of arcs necessary low. The structures of $BN_{ht,l}$ are assessed via the d-calibration score and CvM statistic. For sample sizes of 80 to 300,

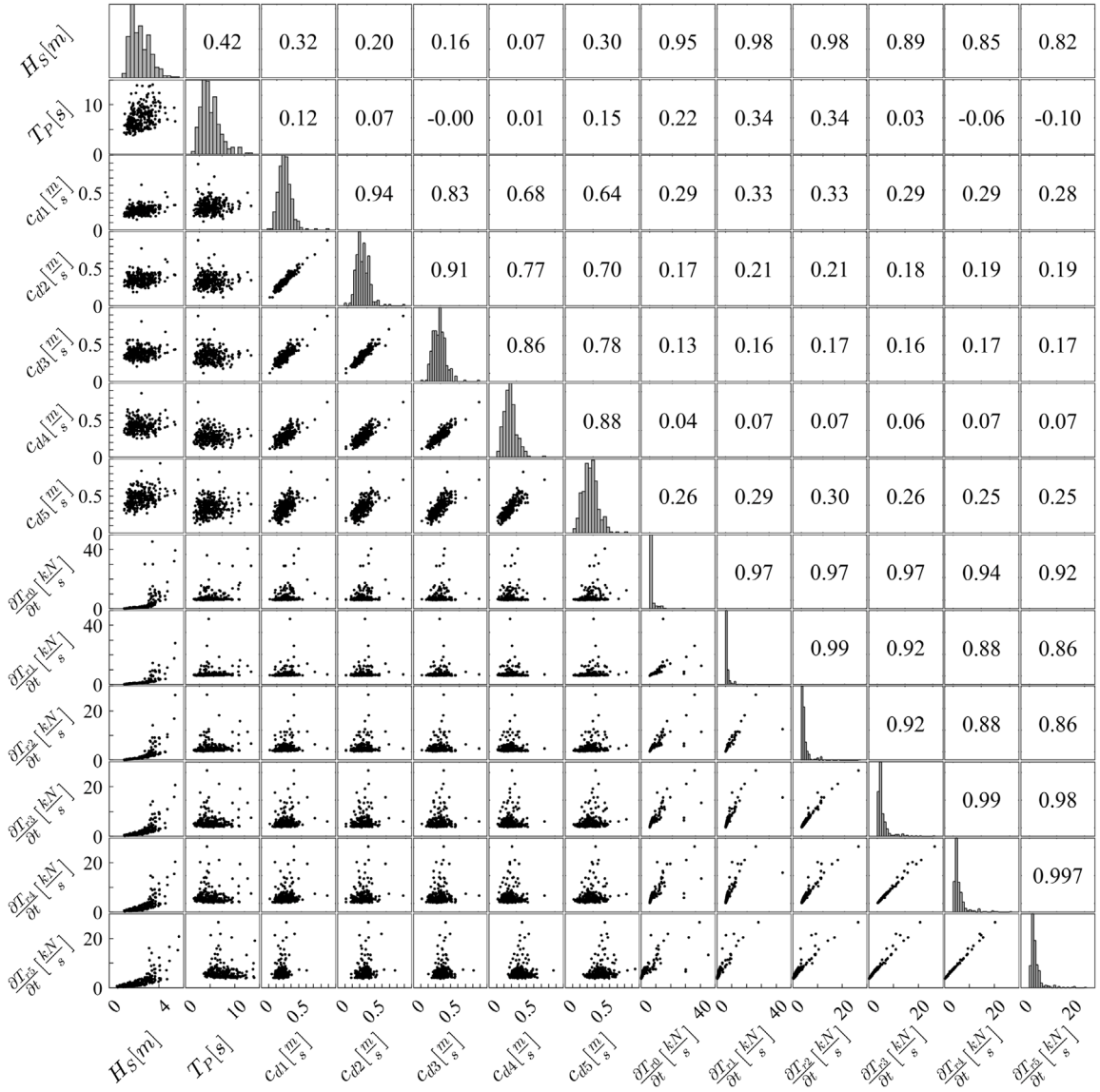

Fig. 6. Pairwise scatter plots of the studied variables in their physical units for RefLoc 4 are presented in the lower-left part, together with their empirical marginal distributions on the diagonal and rank correlation coefficients above the diagonal.

the d-calibration score between the correlation matrix of $BN_{ht,l}$ and the empirical data varies between 0.5 and 0.8. Note however that this method is known to be sensitive to the sample size. The Gaussian copula for each variable pair connected by an arc is additionally verified via the CvM statistics. For the results of CvM among the hydrodynamic variables, see Section 4.1. An example of the empirical data for RefLoc 4, which serves as input for the $BN_{ht,4}$, is given in Fig. 7. For this location, but also other locations with medium distance to shore (3 to 9), it appears that there is some upper tail dependence among the tension rates. According to CvM, however, the joint dependence can be mostly described via the symmetric Gaussian copula, or the Frank copula. For some variable pairs, such as among tension rates, the Gaussian copula fits to a similar degree as the Gumbel copula, or even better. This is the same for the joint dependence structure among currents for location 3.

The correlation matrix of $BN_{ht,l}$ should approximately match the correlation matrix of the empirical data. In addition to the Spearman correlation coefficients ρ, p-values are determined as a measure for statistical significance of ρ. The left side of Fig. 8 shows the correlation matrix for RefLoc 4, while the right side presents the corresponding p-values. Note that for both, top-right above the diagonal black line corresponds to the empirical data, while parts below the line correspond to $BN_{ht,4}$.[1] For the RefLoc 4, all correlation coefficients between the empirical variables for this location are positive, except for the pairs of T_P with the current magnitudes c_{d3} and maxima of tension rates, $\frac{\partial T_{r4-5}}{\partial t}$, both close to the surface. However, these correlations are close to zero and their p-values are > 0.05, thus the correlations are found not to be significant. Generally it can be seen that the correlation matrix of $BN_{ht,4}$, lower left, does match well the correlation matrix of the empirical data, upper-right. Slight difference in the correlations of > 0.1 are observed for RefLoc 4 for the variables pairs of T_P with $\frac{\partial T_{r,0}}{\partial t}$ and $\frac{\partial T_{r,0}}{\partial t}$ with $\frac{\partial T_{r,3}}{\partial t}$. For both, empirical correlation matrix and the one of $BN_{ht,4}$, there are strong correlation coefficients between H_S and tensions rates, as well as among current magnitudes and among tension rates. The p-values in for the empirical data are above thresholds for the variables pairs of H_S with c_{d4} and T_P with current magnitudes and tension rates close to the surface. However, these variable pairs

[1] The rank correlation coefficients and p-values are similar across the selected locations in the North Sea and thus not all are presented in this study, but can be made available upon request.

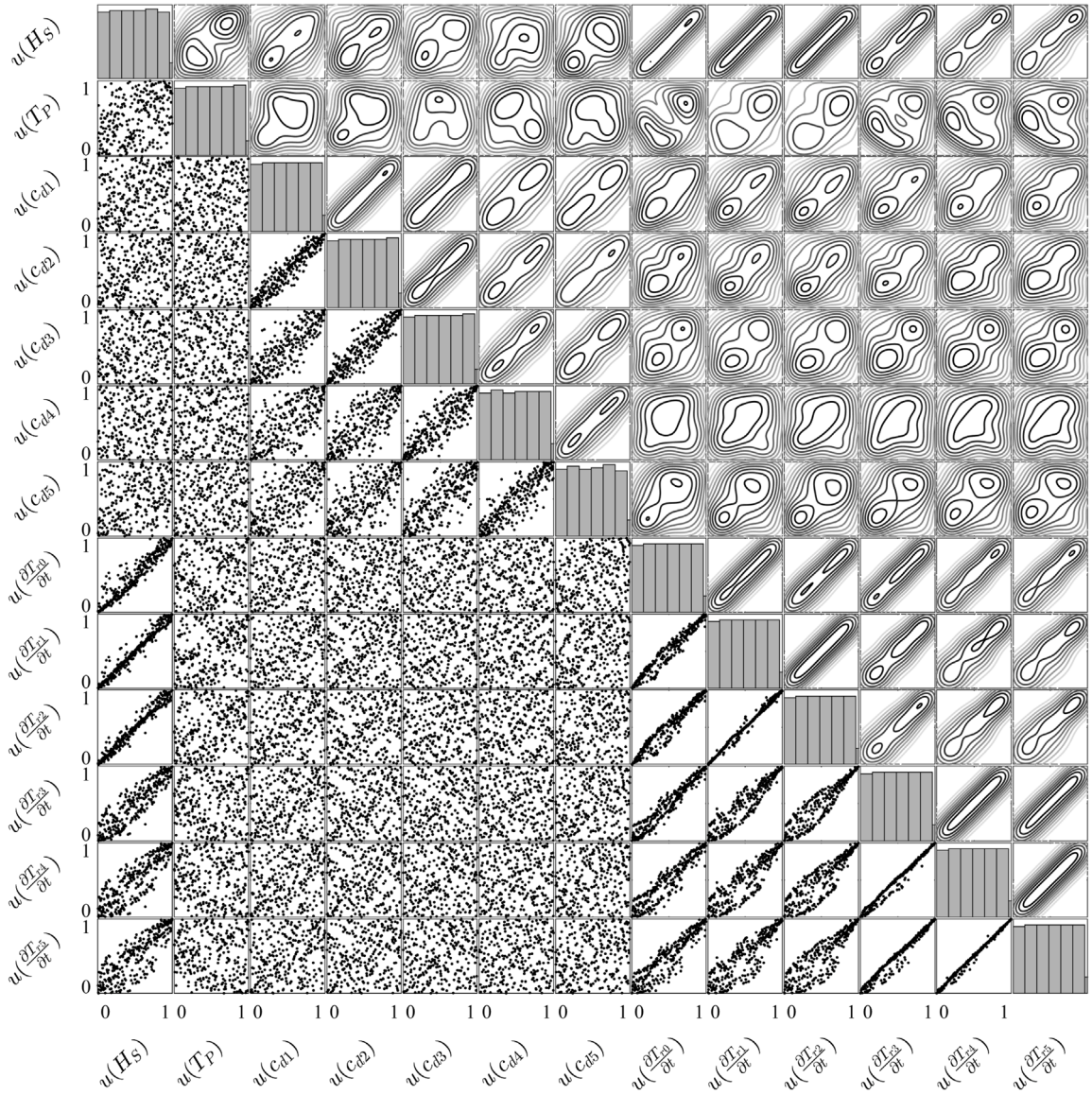

Fig. 7. Pairwise scatter plots of the studied variables transformed to unit space for RefLoc 4 are presented in the lower-left part, together with their one-dimensional uniform margins on the diagonal and their densities as contours above the diagonal.

have very low correlations and are thus not connected by an arc in the $BN_{ht,4}$.

The described characteristics for RefLoc 4 are generally observed across all locations l. However, for locations 2, 3, 5 to 8, and 12, some arcs between variables are needed despite their low correlation linked with a high p-value. Removing these arcs would make the fit worse.

Generally, it is observed that the structure among the tension rates $\frac{\partial T_{r,p}}{\partial t}$ depends on the distance to shore. The structure for the offshore locations 10 to 12 with high water depths is identical. Adding two arcs among the upper tension rates in the rope, the structure becomes identical for the medium-distant locations 4 to 9. Adding two more arcs to this structure among the tension rates T' results in the structure of the near-shore and shallow locations 2 and 3.

4.4. Evaluation of tension rates at various percentiles

The above described structures for each $BN_{ht,l}$ are used to generate $n = 1.000.000$ samples for seven hydrodynamic variables and five tension rate variables per location l in the south-eastern North Sea. These sample sets are used to assess expected tension rates and to investigate the spatial differences across the south-eastern North Sea.

Fig. 9 presents the tension rate values for the 90th percentile across the studied locations, with the left side showing values at the anchor ($r0$) and the right side showing values at the fairlead ($r5$). Thus, thresholds are shown, indicating that 90% of the tension rates in the mooring line fall below these values. As previously mentioned, results for location 1 are not reported, because the mooring line simulations have not been successful due to the insufficient water depth. The background in Fig. 9 indicates the water depths. For detailed information on the water depth in the area, see Fig. 1, and for the precise water depths per location l, see Table 1. The 90th percentile is determined by fitting the generalised extreme value (GEV) distribution to the selected maxima tensions, as described in Section 3.4. Fig. D.14 in Appendix D provides an overview of the maxima of the tension rates at the anchor for RefLoc 4. It compares the empirical cumulative distribution function (cdf) with the cdf of the fitted GEV distribution. The inverse cdf of the GEV is used to determine the value corresponding to a probability of 0.9. The tension rates at the anchor, $\frac{\partial T_{r0}}{\partial t}$, in the left map in Fig. 9 are similar among the locations 9 to 12. These locations have the greatest

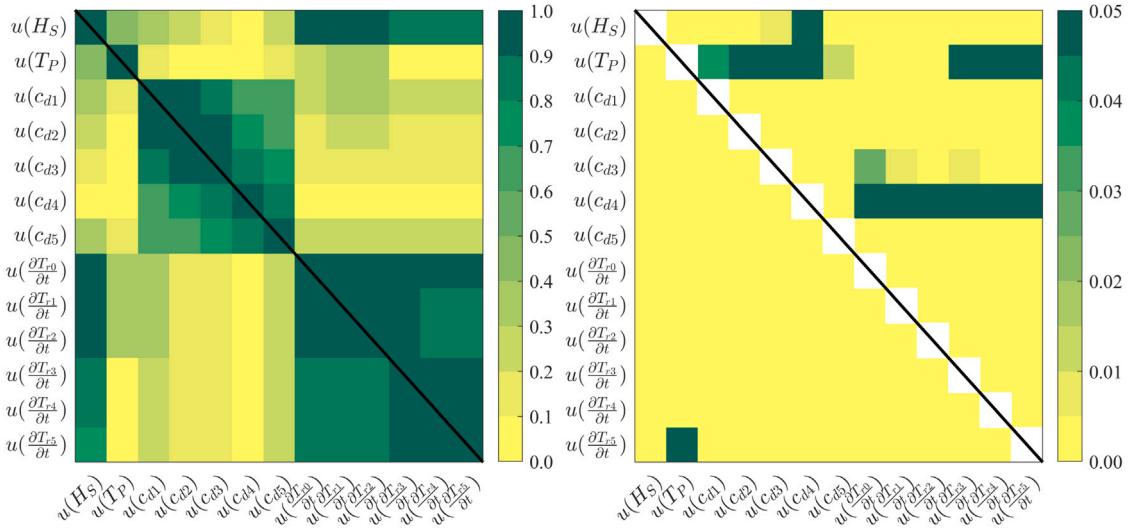

Fig. 8. Left: Spearman's rank correlation coefficients for the studied variables at RefLoc 4. Right: Corresponding p-values. In both plots, values above the black diagonal correspond to empirical data, while those below correspond to data from the GCBNs.

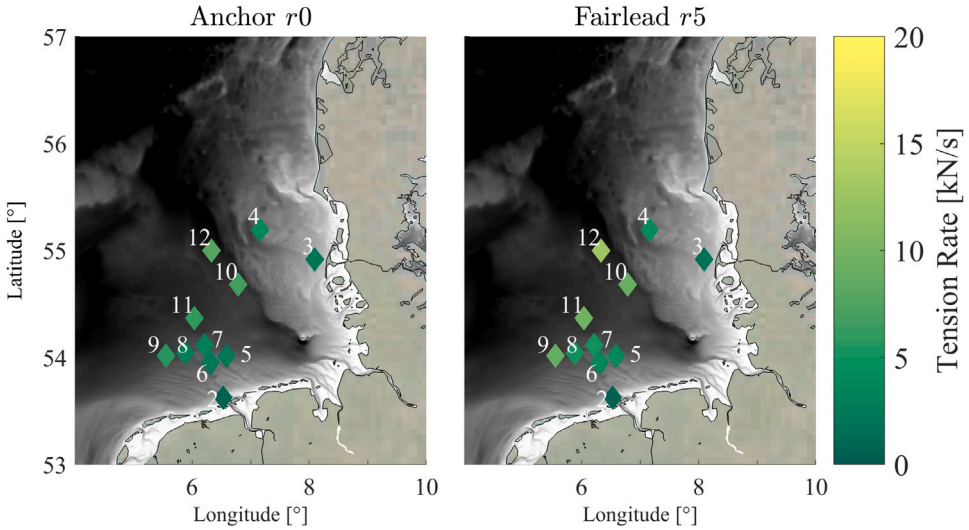

Fig. 9. Design values of tension rates for $P(X \leq 0.9)$ at the anchor (left) and at fairlead (right).

water depth among those studied, with depths exceeding 38.6 m. For the fairlead (right side of Fig. 9), location 12 stands out by experiencing significantly higher tension rates compared to the other locations. This could be due to the water depth, as location 12 is the deepest, with a water depth of about 45 m. Additionally, mooring lines modelled for locations 4 to 8 also exhibit similar tension rates at both the anchor and fairlead, with water depths ranging from 22.8 to 35.7 m. Similarly, the tension rates for the mooring lines at the shallow locations 2 and 3, with depths below 15 m, are also comparable.

Following these observations, the rank correlations between the tension rate values for the 90th percentile and the water depths across the studied locations are calculated. For the anchor, the correlation is 0.83, while for the fairlead, the correlation is found to be 0.91. These high correlations indicate that the water depth is one of the main variables influencing the tension rates in the mooring line.

To better visualise the differences among locations l with increasing depth d, as well as among several positions p in the mooring line, Fig. 10 presents the 90th percentile of tension rate values for three different conditionalisation scenarios, indicated by different markers. These tension rates are calculated for the anchor ($r0$), four intermediate rope locations, and for the fairlead ($r5$). For comparison, the results for the 95th percentile are shown in Fig. E.15 in Appendix E.

The unconditionalised scenario is marked by a triangle ($\triangledown$). The results of this scenario at the anchor (top-left plot of Fig. 10) correspond to the map on the left, while the results of the fairlead correspond to the map plot on the right in Fig. 9. Note that at locations 2 and 3, the water depth is low and thus, the vertical resolution is not sufficient to separate the rope into 6 positions. Therefore, intermediate rope position $r4$ overlaps with the fairlead $r5$, so no data is shown for $r4$ for these locations. For the unconditionalised scenario ($\triangledown$), it can be seen that the differences in tension rates across mooring line positions, p, are generally small. Tension rates appear to be higher at the fairlead $r5$, compared to lower-located rope positions. Locations 2 and 3 are an exception to this due to their low water depth. For the shallow locations 1 to 8, the differences in tension rates for the 90th and 95th percentile for the unconditionalised scenario are comparably small (see Fig. E.15 in Appendix E). This is different for the deeper locations 9 to 12, where the differences in tension rates for the 90th

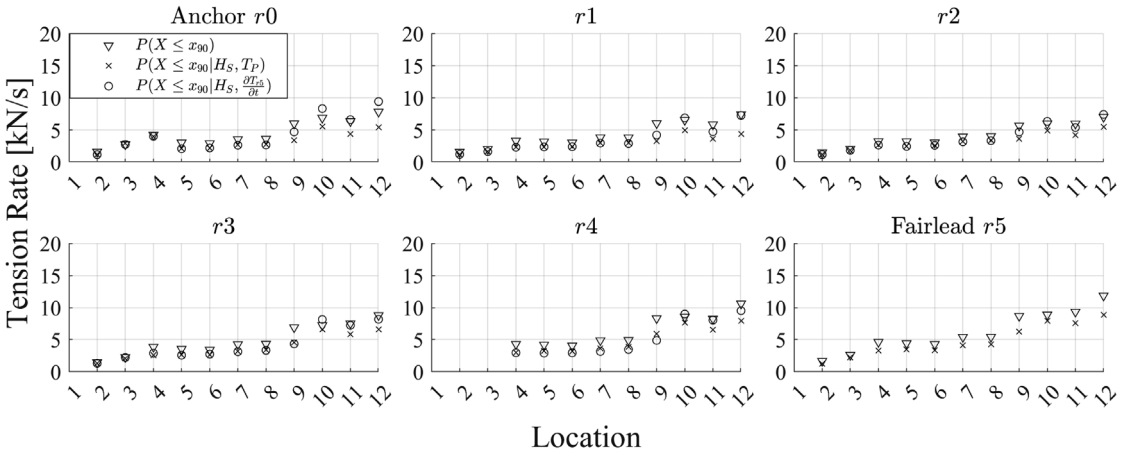

Fig. 10. The 90th-percentile design values of tension rates are presented for six rope positions (r), including the anchor and fairlead, for three conditionalising cases.

and 95th percentile for the unconditionalised scenario marked by ▽ are relatively large, despite using the symmetric Gaussian copula, to generate the sample sets. Therefore, the distribution of tension rates for deep locations appears to have a heavier tail.

Fig. E.16 in Appendix E presents the 90th percentile results, normalised by the static pretension per location l. Similar to the non-normalised Figs. 10 and E.15, a general trend between water depth and tension rate is visible as well, except for two locations. Location 3 and 4, which are relatively shallow with a water depths of 15.0 m and 22.8 m respectively, have significantly higher tension rates, particularly at the anchor, compared to other locations with similar depths. This can be attributed to their exposure to the dominant south to south-west storm direction (Sušelj et al., 2010; de Winter et al., 2013) and the influence of a long wind fetch. Same applies to the deeper locations 9 to 12, whereas locations 1, 2 and 6 to 8 are relatively sheltered by the coastline.

4.5. Evaluation of tension rates for different conditionalisation scenarios

The results above in Section 4.4 are here compared to two conditionalising cases. The power of the GCBN to conditionalise on certain variables is done here for several reasons. First, conditionalising on certain variables provides further insights into the characteristics of the conditioned extreme tension rates and thus helps to assess the reliability of a floating structure under certain conditions. Therefore, by holding certain variables constant, uncertainties in the analysis of extreme tension rates can potentially be reduced. Furthermore, if information about specific variables is available, its impact on tension rates in the mooring lines can be assessed. The two conditionalising cases per location l considered here are:

1. Conditionalising on the 80th percentiles of H_S and T_P
2. Conditionalising on the 80th percentiles of H_S and $\frac{\partial T_{r5}}{\partial t}$

The first case is selected as waves are earlier identified as most influential for the tension rates. Additionally, they are comparably easy to measure. The second case is chosen by assuming that information about the tension at the fairlead is available, e.g. due to an installed sensor between the mooring line and the floating structure. This helps to receive information about rope positions p below the fairlead, including the anchor. Regarding the first case, it is important to note that for the RefLoc 4, conditionalising on T_P has no influence on the tension rates, if H_S is known. This is due to conditional independence

Table 4
80th percentile values for variables used for conditionalisation.

Location l	H_S [m]	T_P [s]	$\frac{\partial T_{r5}}{\partial t}$ [kN/s]
1	–	–	–
2	2.84	8.49	2.88
3	2.63	8.20	1.80
4	2.98	8.73	2.93
5	2.84	8.49	2.88
7	3.11	8.89	3.21
6	2.86	8.60	2.89
8	3.00	8.44	3.35
9	3.16	8.57	5.00
10	3.09	8.74	5.23
11	3.11	8.64	5.77
12	3.34	9.22	7.20

of tension rates and T_P given H_S (see the structure of $BN_{ht,4}$ in Fig. C.13(d) in Appendix C). BANSHEE (Paprotny et al., 2020; Koot et al., 2023) is used to generate sets of $n = 1.000.000$ samples conditionalised on certain variables and values per location l, which are shown in Table 4.

Similar to the results described in Section 4.4 for the unconditionalised case, GEV distributions are fitted to the tension rates and the obtained values corresponding to 90th and 95th percentile are analysed. In Figs. 10 and E.15 in Appendix E, the results for the conditionalising cases 1, indicated by ×, and 2, indicated by ∘, are presented for the 90th and 95th percentiles, respectively. With regard to the water depths, a similar behaviour for the conditionalised tension rates for the 90th percentile is observed compared to the unconditionalised case. The larger the water depth, the higher the 90th percentile of tension rates. Additionally, for most of the locations l and rope positions p, the 90th percentile of conditionalised tension rates are lower than those of the unconditionalised case (marked as ▽). Details of the RefLoc 4 are displayed in Table 5. The reason for these unexpected observations lies in the heavy-tailed distributions of the tension rates. Therefore, there is a (relatively) high probability of extreme values and thus large variance, as the variance is sensitive to the square of the deviations from the mean per variable. By holding certain variables constant at their 80th percentile, extremes are eliminated and thus, the variance of tension rates is reduced and generally (uninventively) lower compared to the unconditionalised case.

The difference between the two conditionalising cases is most significant for the deep locations 9 to 12 (see Fig. E.15 in Appendix E). This is

Table 5
Tension rate values [kN/s] for 90th and 95th percentile for RefLoc 4 for three conditionalisation cases.

	$r0$	$r1$	$r2$	$r3$	$r4$	$r5$
$P(X \leq x_{90})$	4.22	3.31	3.23	3.85	4.30	4.62
$P(X \leq x_{90} \mid H_S, T_P)$	3.95	2.33	2.63	2.61	3.02	3.27
$P(X \leq x_{90} \mid H_S, T_P, \frac{\partial T_{r5}}{\partial t})$	4.01	2.31	2.64	2.87	2.96	–
$P(X \leq x_{95})$	7.42	5.08	5.00	5.80	6.35	6.67
$P(X \leq x_{95} \mid H_S, T_P)$	5.19	2.58	3.00	3.06	3.47	3.71
$P(X \leq x_{95} \mid H_S, T_P, \frac{\partial T_{r5}}{\partial t})$	5.19	2.53	2.98	3.05	3.03	–

similar to the above described results, as the tension rate distributions at these locations seem to have a heavier tail.

Finally, comparing the conditionalising cases 1 and 2, differences in tension rates for the lower rope location r_{0-4} are marginal. Thus in this case, where H_S is found to have the most influence on the tension rates, it is sufficient to conditionalise only on H_S in order to analyse extreme tension rates under specific conditions.

5. Discussion

Gaussian copula-based Bayesian Networks (GCBNs) were used in this study to model the multivariate dependence of hydrodynamic variables, i.e. wave and current variables, and tension rates at different positions in a mooring line. It helped to analyse extreme tension rates as an indicator of snap loads in a mooring line of a floating structure. This was done exemplarily for a seaweed cultivation structure for several different study locations across the south-eastern North Sea, each with different offshore conditions and water depths. The results presented here are, however, transferable to any other floating structure.

Some considerations potentially influencing the results are not addressed in this study. Even though study locations with different water depths are selected, the bathymetry at each location is not considered further. This might be relevant because according to Desiré et al. (2023), accounting for the bathymetry has a significant effect on snap loads. Furthermore, the present study assumes that waves and currents are consistently in-line with the structure. Mooring lines are modelled two-dimensionally on the axes x and z, see Fig. 2. However, this way the complexity of the environment is not fully taken into account (Hermawan and Furukawa, 2020; Feng et al., 2021). Additionally, in this study, one single mooring line is considered, while different tensions are expected for different mooring lines of a floating structure. For example, in aquaculture structures, an increase in biomass results in higher tensions in several lines, particularly in the downstream mooring lines, but reduces the maximum tensions in the upstream mooring lines (Feng et al., 2021).

It was found that influences of hydrodynamic variables on the tensions or tension rates appear to be different for certain conditions. While Nguyen et al. (2019) observed in field experiments that currents significantly influence mooring line tensions in low to mid-tidal levels, this study determined the significant wave height to be the main driver for tensions. However, the average water depths of the field experiments conducted by Nguyen et al. (2019) was 2.5 m. In the presented study, the depths varied between 12.6 to 44.7 m. The correlation between current magnitudes and tension rates was found to be mainly between −0.19 and 0.35, different from the correlation between significant wave heights and tension rates (0.81 to 0.98). Thus for snap loads, the current magnitudes can be neglected, as they are rather relevant for static pre-tensions than snap loads.

This study calculates mooring line tension rates using GCBNs, which account for the multivariate dependence between hydrodynamic variables and tension rates. These results are then compared to tension rates obtained under two conditionalising cases: one conditioned on the 80th percentile of significant wave height (H_S) and peak wave period (T_P), and the other conditioned on H_S and anchor tension rate. At the RefLoc 4, the results for the first conditionalising case are independent of T_P given H_S. Thus, in this specific case it is sufficient to conditionalise only on H_S. Therefore, computational efforts can be minimised given conditional independent variables for certain GCBN structures. Additionally, the results show that tension rates for the two conditionalising cases are lower compared to the unconditionalised case. This can be attributed to the heavy-tailed distributions of the tension rates, as there is a high probability of extreme values. Thus, conditionalising on certain variables leads to an "elimination" of extremes and therefore, both the 90th and 95th percentiles are lower compared to those of the unconditionalised case. Although this was observed in the presence of heavy-tailed tension rate distributions, the mooring line design should be based on a conservative case, considering most extreme tension rates. Uncertainties are reduced when information about specific hydrodynamic variables is available, and conditionalising on this reduces uncertainties leading to increased safety and reliability of the structures.

The structure chosen for this study is based on a pilot case at RefLoc 4. Consequently, as outlined in Section 2.3, the mooring line dimensions for other locations are scaled according to their respective water depths to ensure a consistent surge restoring stiffness across all locations (refer to Table 3). Thus, the results will differ in magnitude for different design parameters or even different moored floating structures, such as offshore wind turbines, vessels or floating solar panels. However, the characteristics are expected to be similar and the method can be applied to any moored floating structure. The method presented here is chosen for several reasons. It not only identifies which hydrodynamic variables significantly influence tension rates but also enables spatial analysis to compare variations across locations and estimate expected tension rates. Additionally, GCBNs offer computational efficiency in modelling the multivariate dependencies among variables, which Montes-Iturrizaga and Heredia-Zavoni (2016) identified as a crucial next step in the reliability assessment of mooring lines, as dependencies among variables often affect failure mechanisms. This has been further shown by using the GCBN to conditionalise on certain variables and analyse the resulting tension rates.

For the GCBN, the Gaussian copula is selected to model the multivariate distribution among variables. The selection of the Gaussian copula might not be the best chosen copula model. The results of Montes-Iturrizaga and Heredia-Zavoni (2016) show that selecting the Gaussian copula model can over- or underestimate the failure probability. In general, the results are sensitive to the choice of copula model. However, the results of the Cramér–von Mises statistic, which was applied as one out of two goodness-of-fit measures (see Sections 4.1 and 4.3), show that the Gaussian copula is a reasonable fit to model the dependence among the studied variables. Additionally, the d-calibration score was used to assess whether the GCBN properly represents the multivariate dependence structure of the selected variables, together with a pairwise correlation comparison (see Section 4.3). Both conclude that the individual GCBN per studied location are a suitable fit to model the multivariate dependence of studied variables. The presented GCBN enables to determine marginal distributions of tension rates influenced by multiple factors, or given specific conditions (see Section 4.5). Thus, GBCN's are employed to quantify the sensitivity of tension rates at different rope positions to certain hydrodynamic factors. Since empirical data is used as input to the GCBNs, the model can be updated given new observations to improve its accuracy. To account for different copula models among variable pairs and also to model tail dependencies such as those observed among tension rates, vine copula models (Joe, 2015; Morales-Nápoles et al., 2023) are a potential next step. However, due to their complexity and fitting all possible structures of vine copula models to the data, they are limited in application to a small number of variables. Considering 13 variables, as done in this study via GCBNs, would make the investigation of all possible vine copulas for the data unfeasible.

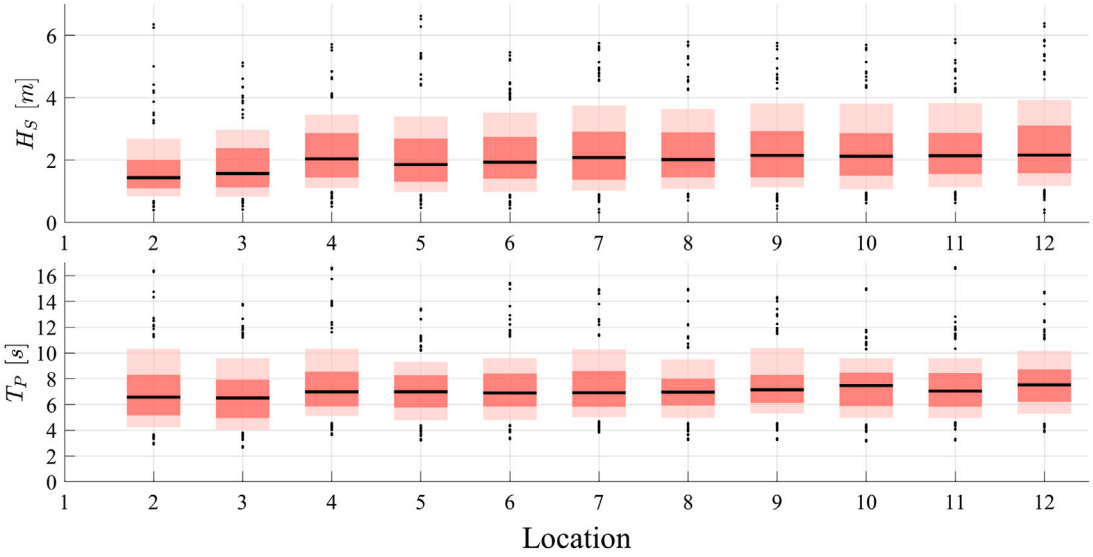

Fig. A.11. Overview of significant wave height (H_S) and peak wave period (T_P) distributions for each location l. Light red shading represents the 10th–90th percentile range, dark red shading represents the 25th–75th percentile range, and the median is indicated by a black horizontal line. (For interpretation of the references to colour in this figure legend, the reader is referred to the web version of this article.)

6. Conclusion

Gaussian copula-based Bayesian Networks (GCBNs) have been used in this study to model the multivariate dependence and thus the influence of hydrodynamic variables on the tension rates in a mooring line of a floating structure. This has been done to gain more understanding of critical snap loads, which put the structure at risk.

The presented method allows for inference for unconditional and conditionalising cases. GCBNs rely on a single one-parameter copula, which is the Gaussian copula.

It has been applied at 12 study locations, conditionalising on variables highly correlated with tension rates, which have an effect on the marginal distributions of the tension rates. This approach is particularly of advantage when data for such variables are available, as it reduces uncertainty in predicting tension rates under specific conditions. The results show that conditionalising on harsh hydrodynamic conditions, the snap loads are counter-intuitively lower due to their heavy-tailed marginal distributions. This highlights the need to account for the dependence among hydrodynamic variables and tension rates, to improve structures' safety.

The current study establishes a framework for constructing a Bayesian Network that correlates sea state conditions with mooring line tension. The analysis was conducted under a simplified assumption that the floater moves with the wave particles. This assumption facilitates reproducibility and ensures that the analysis is not constrained by specific floater properties. In future work, we intend to extend the Bayesian Network to incorporate floater properties and their corresponding dynamic responses. These properties will serve as additional inputs to the network, enabling a more comprehensive and realistic representation of the system behaviour.

CRediT authorship contribution statement

R. Santjer: Writing – original draft, Writing – review & editing, Formal analysis, Methodology, Conceptualization. **S. Agarwal:** Writing – review & editing, Writing – original draft, Methodology. **O. Colomés:** Writing – review & editing. **O. Morales-Nápoles:** Writing – review & editing, Conceptualization.

Declaration of competing interest

The authors declare that they have no known competing financial interests or personal relationships that could have appeared to influence the work reported in this paper.

Acknowledgements

The first author acknowledges Stichting Deltares for providing financial support for this study. The authors acknowledge the use of Snellius, the National Supercomputer, hosted by SURF, and the Delft-Blue supercomputer, hosted by Delft High Performance Computing Centre (https://www.tudelft.nl/dhpc), for providing the computational resources required for this work.

Appendix A. Overview of wave characteristics

See Fig. A.11.

Appendix B. Example hydrodynamic model data

See Fig. B.12.

Appendix C. GCBN structures for each study location

See Fig. C.13.

Appendix D. Comparison of cumulative distribution functions

See Fig. D.14.

Appendix E. Additional results on tension rate percentiles

See Figs. E.15 and E.16.

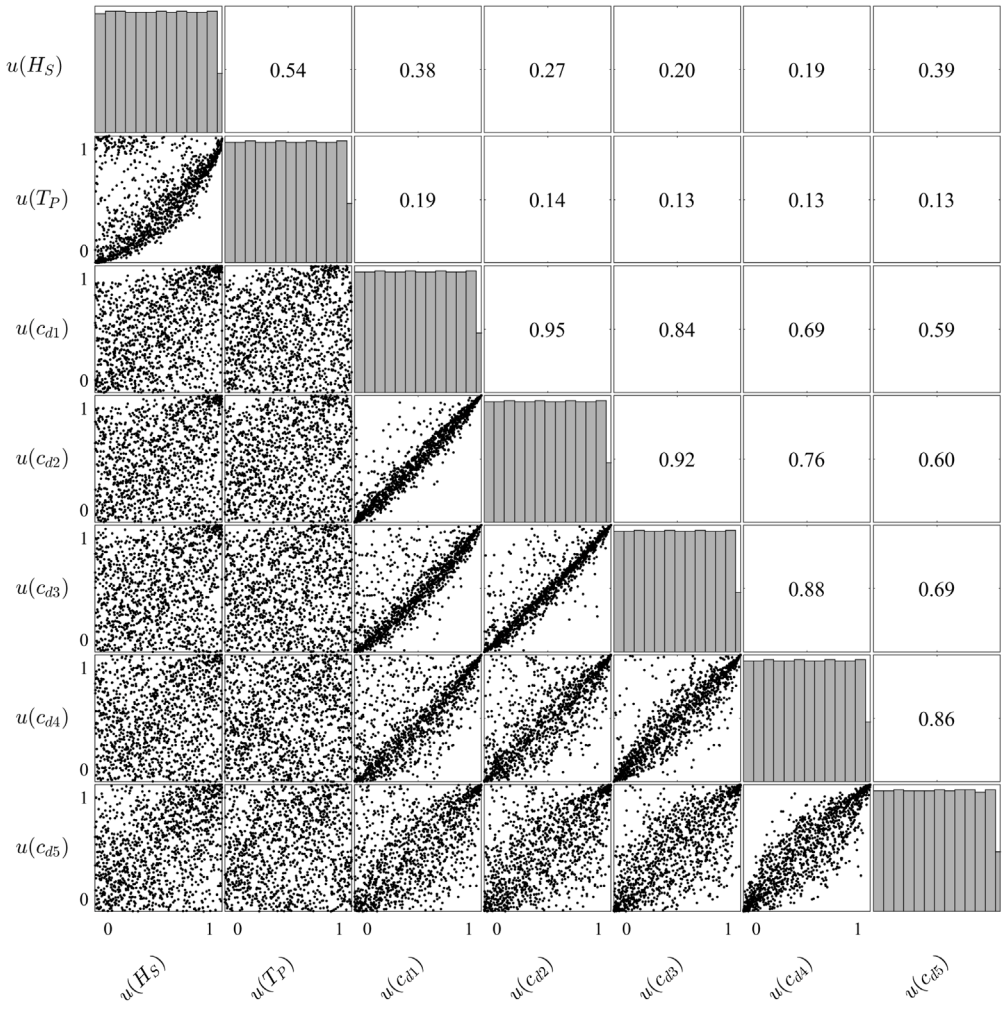

Fig. B.12. Pairwise scatter plots of the data from the hydrodynamic model (DCSM) transformed to unit space for RefLoc 4 are presented in the lower-left part, together with their one-dimensional uniform margins on the diagonal and rank correlation coefficients above the diagonal. This hydrodynamic data serves as input for $BN_{h,l}$.

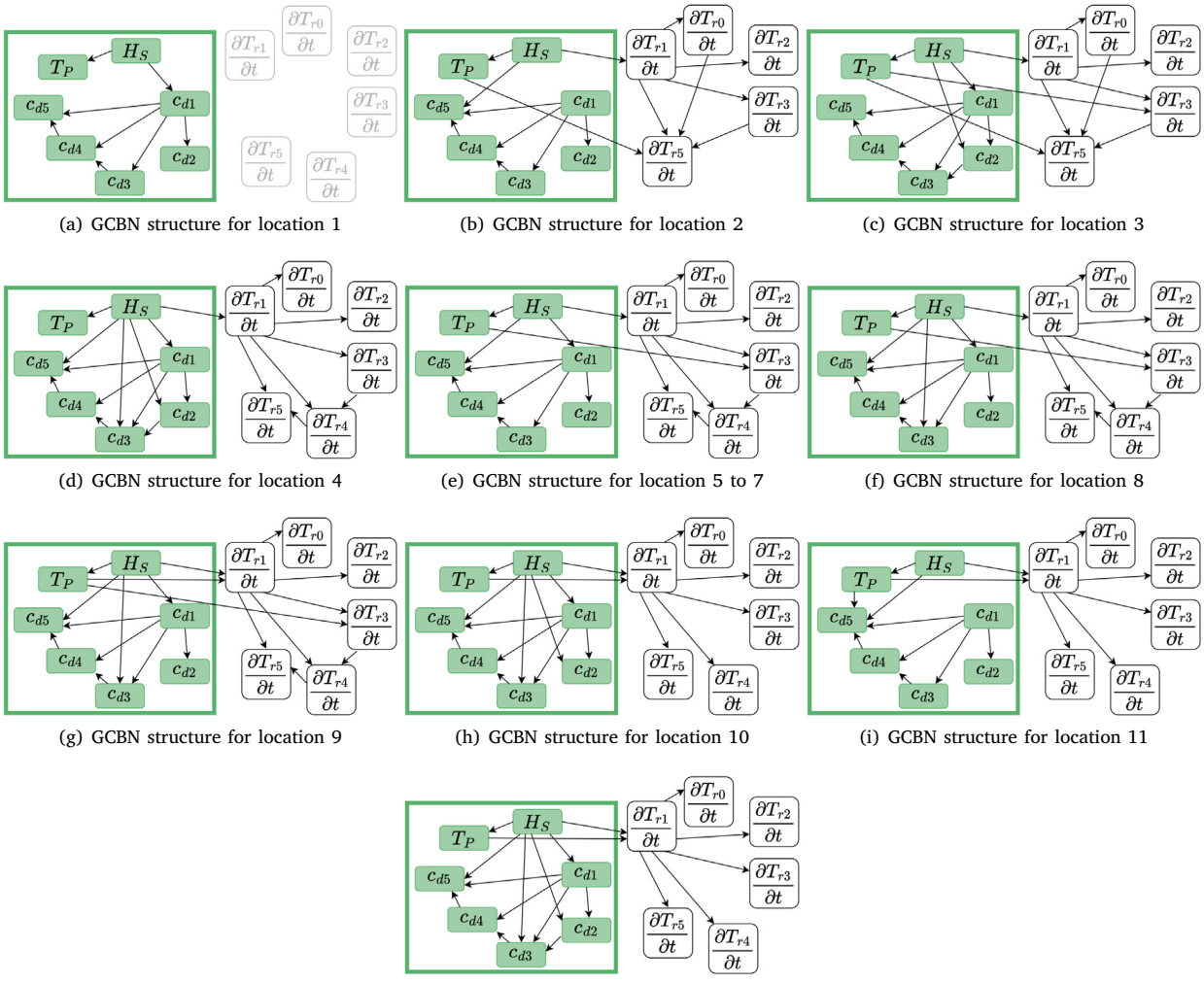

(a) GCBN structure for location 1 (b) GCBN structure for location 2 (c) GCBN structure for location 3

(d) GCBN structure for location 4 (e) GCBN structure for location 5 to 7 (f) GCBN structure for location 8

(g) GCBN structure for location 9 (h) GCBN structure for location 10 (i) GCBN structure for location 11

(j) GCBN structure for location 12

Fig. C.13. Structure of the GCBNs for each studied location l. The hydrodynamic $BN_{h,l}$, marked in green on the left, are extended by tension rates to receive $BN_{ht,l}$, presented here.

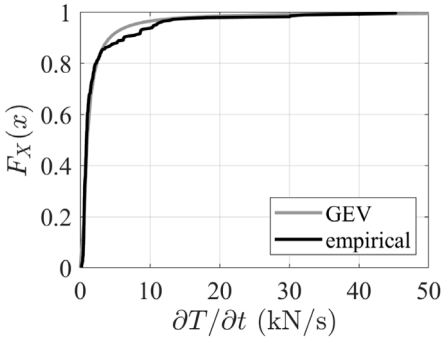

Fig. D.14. Comparison of the empirical cumulative distribution function (cdf) for the tension rate at the anchor, derived from $BN_{ht,l}$ with $n = 1{,}000{,}000$ samples, against the cdf of a fitted Generalised Extreme Value (GEV) distribution for RefLoc 4.

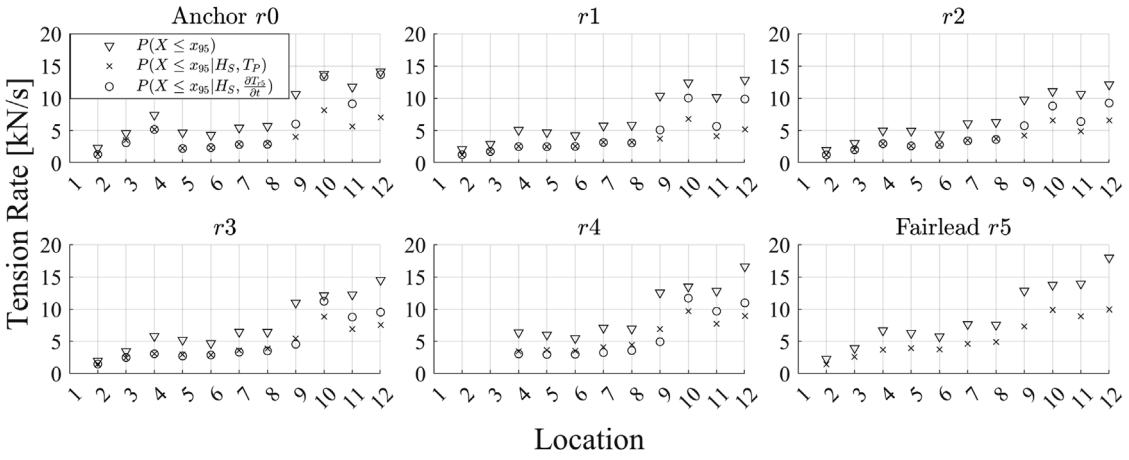

Fig. E.15. The 95th-percentile design values of tension rates are presented for six rope positions (r), including the anchor and fairlead, for three conditionalising cases.

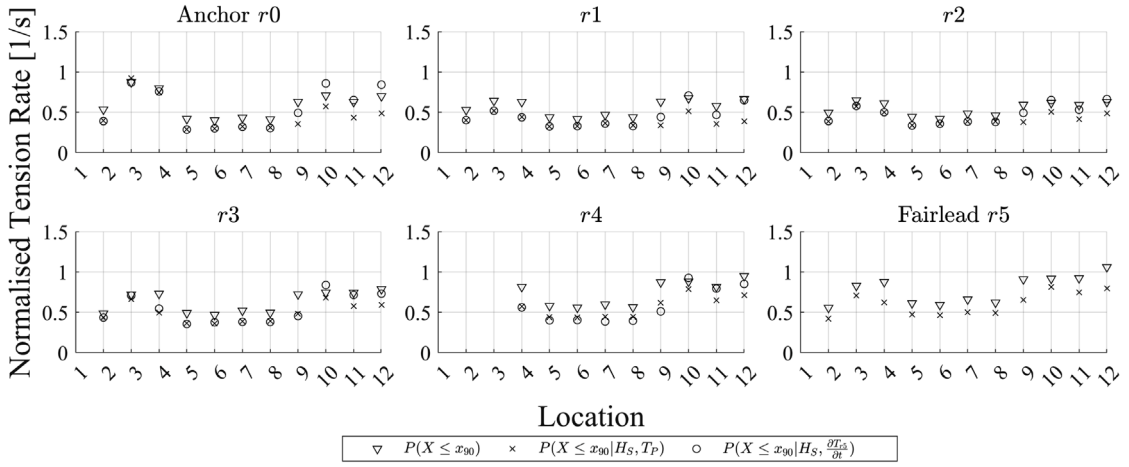

Fig. E.16. The 90th-percentile design values of tension rates, normalised by their static pretension, are presented for six rope positions (r), including the anchor and fairlead, for three conditionalising cases.

References

Agarwal, S., Gomez, S., Colomes Gene, O., 2025. Dynamic finite-strain analysis of mooring lines based on tangential differential calculus. preprint. http://dx.doi.org/10.2139/ssrn.5271454.

Barros, B., Conde, B., Riveiro, B., Morales-Nápoles, O., 2024. Gaussian copula-based Bayesian network approach for characterizing spatial variability in aging steel bridges. Struct. Saf. 106, 102403. http://dx.doi.org/10.1016/j.strusafe.2023.102403.

Bergdahl, L., Palm, J., Eskilsson, C., Lindahl, J., 2016. Dynamically scaled model experiment of a mooring cable. J. Mar. Sci. Eng. 4 (1), 5. http://dx.doi.org/10.3390/jmse4010005.

Booij, N., Ris, R., Holthuijsen, L., 1999. A third-generation wave model for coastal regions, part I, model description and validation. J. Geophys. Res. 104, 7649–7656.

Buck, B.H., 2002. Open Ocean Aquaculture und Offshore-Windparks: Eine Machbarkeitsstudie über die multifunktionale Nutzung von Offshore-Windparks und Offshore-Marikultur im Raum Nordsee. Rep. Polar Mar. Res. 254,

Buck, B.H., Langan, R., 2017. Aquaculture perspective of multi-use sites in the open ocean. http://dx.doi.org/10.1007/978-3-319-51159-7.

Buck, B.H., Troell, M.F., Krause, G., Angel, D.L., Grote, B., Chopin, T., 2018. State of the art and challenges for offshore integrated multi-trophic aquaculture (IMTA). Front. Mar. Sci. 5, http://dx.doi.org/10.3389/fmars.2018.00165.

Chung, J., Hulbert, G.M., 1993. A time integration algorithm for structural dynamics with improved numerical dissipation: The generalized-alpha method. J. Appl. Mech. 60 (2), 371–375. http://dx.doi.org/10.1115/1.2900803.

de Winter, R.C., Sterl, A., Ruessink, B.G., 2013. Wind extremes in the north sea basin under climate change: An ensemble study of 12 CMIP5 GCMs. J. Geophys. Res.: Atmospheres 118 (4), http://dx.doi.org/10.1002/jgrd.50147.

Deltares, 2023. D-FLOW flexible mesh. User manual, deltares.

Desiré, P., Rodríguez-Luis, Á., Guanche, R., 2023. Simulation of mooring lines in complex bathymetries using a finite element method. Ocean Eng. 272, 113827. http://dx.doi.org/10.1016/j.oceaneng.2023.113827.

Dueñas-Osorio, L., Basu, B., 2008. Unavailability of wind turbines due to wind-induced accelerations. Eng. Struct. 30 (4), 885–893. http://dx.doi.org/10.1016/j.engstruct.2007.05.015.

Feng, D., Meng, A., Wang, P., Yao, Y., Gui, F., 2021. Effect of design configuration on structural response of longline aquaculture in waves. Appl. Ocean Res. 107, 102489. http://dx.doi.org/10.1016/j.apor.2020.102489.

Fisher, R., Tippett, L., 1928. Limiting forms of the frequency distribution of the largest or smallest member of a sample. Proc. Camb. Philos. Soc. 24, 180–190. http://dx.doi.org/10.1017/S0305004100015681.

Fries, T., Schöllhammer, D., 2020. A unified finite strain theory for membranes and ropes. Comput. Methods Appl. Mech. Engrg. 365, 113031. http://dx.doi.org/10.1016/j.cma.2020.113031.

Gagnon, M., Bergeron, P., 2017. Observations of the loading and motion of a submerged mussel longline at an open ocean site. Aquac. Eng. 78, 114–129. http://dx.doi.org/10.1016/j.aquaeng.2017.05.004.

Genest, C., Favre, A.-C., 2007. Everything you always wanted to know about copula modeling but were afraid to ask. J. Hydrol. Eng. 347–368. http://dx.doi.org/10.1061/ASCE1084-0699200712:4347.

Genest, C., Rémillard, B., Beaudoin, D., 2009. Goodness-of-fit tests for copulas: A review and a power study. Insurance Math. Econom. 44, 199–213. http://dx.doi.org/10.1016/j.insmatheco.2007.10.005.

Governo, A., Henriques, J., Gato, L., 2023. Modelling mooring line snap loads using a high-order finite-volume approach. Ocean Eng. 275, 113803. http://dx.doi.org/10.1016/j.oceaneng.2023.113803.

Guo, S., Li, Y., Li, M., Chen, W., Fu, Y., 2017. Dynamic response of floating wind turbine under consideration of dynamic behavior of catenary mooring-lines. Proc. Int. Conf. Offshore Mech. Arct. Eng. - OMAE 10, http://dx.doi.org/10.1115/OMAE2017-61689.

Hall, M., Goupee, A., 2015. Validation of a lumped-mass mooring line model with DeepCwind semisubmersible model test data. Ocean Eng. 104, 590–603. http://dx.doi.org/10.1016/j.oceaneng.2015.05.035.

Hanea, A.M., Kurowicka, D., Cooke, R.M., 2006. Hybrid method for quantifying and analyzing Bayesian belief nets. Qual. Reliab. Eng. Int. 22, 709–729. http://dx.doi.org/10.1002/qre.808.

Hanea, A., Morales Napoles, O., Ababei, D., 2015. Non-parametric Bayesian networks: Improving theory and reviewing applications. Reliab. Eng. Syst. Saf. 144, 265–284. http://dx.doi.org/10.1016/j.ress.2015.07.027, URL: https://www.sciencedirect.com/science/article/pii/S0951832015002331.

Hermawan, Y.A., Furukawa, Y., 2020. Coupled three-dimensional dynamics model of multi-component mooring line for motion analysis of floating offshore structure. Ocean Eng. 200, 106928. http://dx.doi.org/10.1016/j.oceaneng.2020.106928.

Hsu, W.-Y., Chuang, T.-C., Yang, R.-Y., Hsu, W.-T., Thiagarajan, K.P., 2019. An experimental study of mooring line damping and snap load in shallow water. J. Offshore Mech. Arct. Eng. 141 (5), 051603. http://dx.doi.org/10.1115/1.4042535.

Hsu, W., Thiagarajan, K.P., Manuel, L., 2017. Extreme mooring tensions due to snap loads on a floating offshore wind turbine system. Mar. Struct. 55, 182–199. http://dx.doi.org/10.1016/j.marstruc.2017.05.005, URL: https://www.sciencedirect.com/science/article/pii/S0951833917300886.

Joe, H., 2015. Dependence Modeling with Copulas. Monographs on Statistics and Applied Probability, vol. 134, CRC Press, Boca Raton, ISBN: 9781466583238, http://dx.doi.org/10.1201/b17116.

Knysh, A., Tsukrov, I., Chambers, M., Swift, M.R., Sullivan, C., Drach, A., 2020. Numerical modeling of submerged mussel longlines with protective sleeves. Aquac. Eng. 88, 102027. http://dx.doi.org/10.1016/j.aquaeng.2019.102027.

Koot, P., Mendoza-Lugo, M.A., Paprotny, D., Morales-Nápoles, O., Ragno, E., Worm, D.T., 2023. Pybanshee version (1.0): A python implementation of the MATLAB toolbox BANSHEE for non-parametric Bayesian networks with updated features. SoftwareX 21, http://dx.doi.org/10.1016/j.softx.2022.101279.

Li, H., Du, J., Wang, S., Sun, M., Chang, A., 2016. Investigation on the probabilistic distribution of mooring line tension for fatigue damage assessment. Ocean Eng. 124, 204–214. http://dx.doi.org/10.1016/j.oceaneng.2016.07.024.

Maar, M., Holbach, A., Boderskov, T., Thomsen, M., Buck, B.H., Kotta, J., Bruhn, A., 2023. Multi-use of offshore wind farms with low-trophic aquaculture can help achieve global sustainability goals. Commun. Earth Environ. 4, 447. http://dx.doi.org/10.1038/s43247-023-01116-6.

Mendoza-Lugo, M.A., Morales-Nápoles, O., 2023. Version 1.3-BANSHEE—A MATLAB toolbox for non-parametric Bayesian networks. SoftwareX 23, 101479. http://dx.doi.org/10.1016/j.softx.2023.101479.

Miškov, V., Dragić, M., Tomin, V., Hofman, M., 2023. Sea trials of sigma wave energy converter – slacking and snapping of TLP mooring lines. Mar. Struct. 89, 103378. http://dx.doi.org/10.1016/j.marstruc.2023.103378, URL: https://www.sciencedirect.com/science/article/pii/S0951833923000114.

Montes-Iturrizaga, R., Heredia-Zavoni, E., 2016. Reliability analysis of mooring lines using copulas to model statistical dependence of environmental variables. Appl. Ocean Res. 59, 564–576. http://dx.doi.org/10.1016/j.apor.2016.07.008.

Morales-Nápoles, O., Delgado-Hernández, D.J., De-León-Escobedo, D., Arteaga-Arcos, J.C., 2014. A continuous Bayesian network for earth dams' risk assessment: Methodology and quantification. Struct. Infrastruct. Eng. 10 (5), 589–603. http://dx.doi.org/10.1080/15732479.2012.757789.

Morales-Nápoles, O., Rajabi-Bahaabadi, M., Torres-Alves, G.A., 't Hart, C.M.P., 2023. Chimera: An atlas of regular vines on up to 8 nodes. Sci. Data 10, 337. http://dx.doi.org/10.1038/s41597-023-02252-6.

Nasyrlayev, N., Dyson, A.P., Kefayati, G., Tolooiyan, A., 2023. Modelling the response of offshore aquaculture fish pens to environmental loads in high-energy regions. Appl. Ocean Res. 135, 103541. http://dx.doi.org/10.1016/j.apor.2023.103541.

Nelsen, R., 2006. An Introduction to Copulas, second ed. Springer Series in Statistics.

Nguyen, N.Q., Thiagarajan, K., Auger, J., 2019. Integrity assessment of an oyster farm mooring system through in-situ measurements and extreme environment modeling. Ocean Eng. 172, 641–659. http://dx.doi.org/10.1016/j.oceaneng.2018.11.023.

Osman, A.I., Chen, L., Yang, M., Msigwa, G., Farghali, M., Fawzy, S., Rooney, D.W., Yap, P.-S., 2023. Cost, environmental impact, and resilience of renewable energy under a changing climate: a review. Environ. Chem. Lett. 21 (2), 741–764. http://dx.doi.org/10.1007/s10311-022-01532-8.

Paprotny, D., Morales-Nápoles, O., Worm, D., Ragno, E., 2020. BANSHEE–A MATLAB toolbox for non-parametric Bayesian networks. SoftwareX 12, http://dx.doi.org/10.1016/j.softx.2020.100588.

Pearson, K., Galton, F., 1895. VII. Note on regression and inheritance in the case of two parents. Proc. R. Soc. Lond. 58 (347–352), 240–242. http://dx.doi.org/10.1098/rspl.1895.0041.

Pickands, J., 1975. Statistical inference using extreme order statistics. Ann. Statist. 3, 119–131. http://dx.doi.org/10.1214/aos/1176343003.

Pınarbaşı, K., Galparsoro, I., Borja, Á., Stelzenmüller, V., Ehler, C.N., Gimpel, A., 2017. Decision support tools in marine spatial planning: Present applications, gaps and future perspectives. Mar. Policy 83, 83–91. http://dx.doi.org/10.1016/j.marpol.2017.05.031.

Santjer, R., Mares-Nasarre, P., Vilmin, L., El Serafy, G., Morales-Nápoles, O., 2024. A probabilistic framework for offshore aquaculture suitability assessment using bivariate copulas. Aquac. Eng. 107, 102479. http://dx.doi.org/10.1016/j.aquaeng.2024.102479.

Sklar, A., 1959. Fonctions de répartition à n dimensions et leurs marges. Publ. L'Inst. Stat. L'Univ. Paris 8.

Soares-Ramos, E.P., de Oliveira-Assis, L., Sarrias-Mena, R., Fernández-Ramírez, L.M., 2020. Current status and future trends of offshore wind power in europe. Energy 202, http://dx.doi.org/10.1016/j.energy.2020.117787.

Somoano, M., Rodríguez-Luis, A., Blanco, D., Guanche, R., 2024. Effect of bathymetry irregularities on the energy dissipation of a mooring line. Ocean Eng. 296, 116932. http://dx.doi.org/10.1016/j.oceaneng.2024.116932.

Spearman, C., 1987. The proof and measurement of association between two things. Am. J. Psychol. 100, 441–471. http://dx.doi.org/10.2307/1422689.

Strothotte, A., Jaeger, M., Pforth, J., Declercq, A., Stechele, B., Nevejan, N., Knoop, J., Kerkhove, T., Petit, S., Pribadi, A., Fernandez, G.V., Lataire, E., Groenendaal, B., Drigkopoulou, I., Brouwers, E., Sørensen, H., Triest, J., 2021. Blueprint for the Offshore Site Operation. Deliverable 7.2, UNITED project: multi-Use platforms and co-locatioN Pilots boostIng cost-effecTive, and Eco-friendly and sustainable proDuction in marine environments, URL: https://www.h2020united.eu/images/PDF_Reports/D72_blueprint_for_the_offshore_site_operation_v30220224.pdf.

Sušelj, K., Sood, A., Heinemann, D., 2010. North sea near-surface wind climate and its relation to the large-scale circulation patterns. Theor. Appl. Climatol. 99, http://dx.doi.org/10.1007/s00704-009-0149-2.

Wu, J., Yu, Y., Cheng, S., Li, Z., Yu, J., 2022. Probabilistic multilevel robustness assessment framework for a TLP under mooring failure considering uncertainties. Reliab. Eng. Syst. Saf. 223, 108458. http://dx.doi.org/10.1016/j.ress.2022.108458.

Xu, S., Guedes Soares, C., 2021. Mixture distribution model for extreme mooring tension and mooring fatigue analysis due to snap loads. Ocean Eng. 234, 109245. http://dx.doi.org/10.1016/j.oceaneng.2021.109245.

Xu, S., yan Ji, C., Guedes Soares, C., 2022. A semiparametric Bayesian method with birth-death Markov chain Monte Carlo algorithm for extreme mooring tension analysis. Ocean Eng. 260, 111765. http://dx.doi.org/10.1016/j.oceaneng.2022.111765.

Yong, W.T.L., Thien, V.Y., Rupert, R., Rodrigues, K.F., 2022. Seaweed: A potential climate change solution. Renew. Sustain. Energy Rev. 159, http://dx.doi.org/10.1016/j.rser.2022.112222.

Zar, J.H., 1972. Significance testing of the spearman rank correlation coefficient. J. Amer. Statist. Assoc. 67 (339), 578–580. http://dx.doi.org/10.1080/01621459.1972.10481251.

Zhao, Y., Dong, S., 2023. Uncertainty analysis of extreme mooring loads associated with environmental contours and peak tension distributions. Mar. Struct. 89, 103369. http://dx.doi.org/10.1016/j.marstruc.2023.103369.

Zijl, F., Zijlker, T., Laan, S., Groenenboom, J., 2023. 3D DCSM FM: A Sixth-Generation Model for the Nw European Shelf. Technical Report, Deltares.